LITERATURE REVIEW OF TSUNAMI SOURCES AFFECTING TSUNAMI HAZARD ALONG THE US EAST COAST

STEPHAN T. GRILLI, JEFFREY C. HARRIS AND TAYEBEH TAJALLI BAKHSH

DEPARTMENT OF OCEAN ENGINEERING, UNIVERSITY OF RHODE ISLAND
NARRAGANSETT, USA

RESEARCH REPORT NO. CACR-11-08
FEBRUARY 2011

CENTER FOR APPLIED COASTAL RESEARCH

Ocean Engineering Laboratory
University of Delaware
Newark, Delaware 19716

TABLE OF CONTENTS

1. BACKGROUND

The University of Delaware and the University of Rhode Island have been funded since 2010 by NOAA's NTHMP program, to perform model simulations of tsunami generation, propagation and impact on the U.S. east coast, in order to establish tsunami inundation maps in regions of elevated hazard or in areas deemed at higher risk. Such studies first require to identify, select, and parameterize, relevant tsunami sources (both distant and local) in the Atlantic Ocean basin, which govern East coast tsunami hazard. This is particularly important for densely populated low-lying areas, which may be highly vulnerable to tsunami impact.

In the Pacific Ocean basin, tsunami hazard assessment, along the U.S. West coast, Alaska, and Hawaii, has long been studied on the basis of substantial historical records of relatively frequent tsunamis. While much fewer records of historical tsunamis exist for the U.S. East coast, it is believed that about 10 percent of tsunami events that have affected the U.S. originated in the Atlantic basin (i.e., Atlantic, Gulf of Mexico, Puerto Rico, the lesser Antilles, and Virgin Islands; see Dunbar and Weaver, 2008). Not much is known, however, about their related coastal hazard (not to mention their return periods).
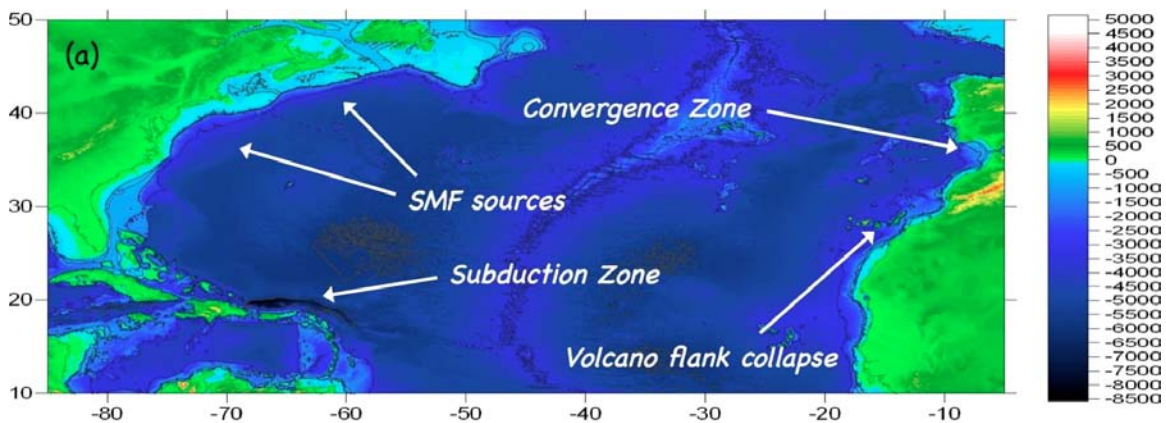
Fig. 1: Potential tsunami sources for U.S. east coast in the North Atlantic Ocean basin (ETOPO2's two second arc length ocean bathymetry is shown in the background).

Historical tsunami events in the Atlantic Ocean basin, that can affect the U.S. East coast, include (Fig. 1):
1. transoceanic co-seismic tsunamis, caused by earthquakes in the Azores-Gibraltar convergence zone (e.g., Lisbon earthquake in 1755; Barkan et al., 2009);
2. transoceanic co-seismic tsunamis, caused by earthquakes along the Hispaniola-Puerto Rico-Lesser Antilles (a.k.a., Caribbean) subduction zone, in and around the Puerto Rico Trench (PRT) or near the Leeward Islands (see, e.g., Grilli et al., 2008; 2010a);
3. a transoceanic landslide tsunami caused by a large mass failure event: the potential flank collapse of the Cumbre Vieja Volcano in the Canary Islands (see, e.g., Ward and Day, 2001; Grilli et al., 2006; Pérignon, 2006; Gisler, 2006; Løvholt et al., 2008; Abadie et al., 2009, 2011).

4. landslide tsunamis caused by Submarine Mass Failures (SMF), triggered along the East coast continental slope by moderate seismic activity. Earlier field and modeling work (tenBrink et al., 2007, 2008, 2009a; Grilli et al., 2006, 2009), indeed, indicates that the most significant tsunami hazard for the U.S. East coast may result from such near-field landslide tsunami sources, which although less energetic than large co-seismic tsunamis, could occur at a short distance from shore (in terms of tsunami propagation time) and hence cause significant runup on small sections of the coast while offering little warning time, thus posing significant hazard to local, low-lying, coastal communities.

2. LITERATURE REVIEW OF RELEVANT TSUNAMI SOURCES

In this report, we focus less on specific events and more on information about potential sources required to setup numerical models of tsunami generation and propagation, with which to study which tsunami sources (and their parameters) may govern tsunami hazard (in terms of runup and inundation) along the U.S. East coast. In a later phase of our work we will quantify this hazard through numerical simulations in a series of nested model grids, for various coastal communities deemed important or identified to be at higher risk, in the form of detailed inundation maps.

For information on specific historical events and a brief history of tsunamis in the Caribbean sea, see, e.g., Lockridge et al. (2002), which includes a catalog of 40 different tsunami or tsunami-like waves that have struck the U.S. East coast since 1600, and Lander et al (2002) who catalogued 91 reports of waves that may have been tsunamis since 1498. Recent studies commissioned by the Nuclear Regulatory Commission, have also been conducted by the USGS, regarding potential tsunami sources affecting the U.S. East Coast (ten Brink, 2007, 2008). Additionally, the NOAA Forecast Source Database (http://nctr.pmel.noaa.gov/propagation-database-access.html) provides a distant source catalog, for the purpose of inundation modeling, recognizing that the depiction of potential tsunami sources will evolve and change with time and that, due to its lower perceived risk, the Atlantic ocean is not very well covered.

In the following, we detail available data for each type of tsunami sources governing the U.S. East coast tsunami hazard (Fig. 1).

2.1 Submarine Mass Failures

Submarine Mass Failures (SMFs), when tsunamigenic, yield potential near-field tsunamis sources that may govern tsunami hazard along the entire U.S. East coast. Although only a few historical landslide tsunamis have been clearly identified in the region, ten Brink et al. (2007) and Twichell et al. (2009) report that one third of the New England continental slope and rise is covered with landslide scars and deposits. Based on their detailed description of field data (see, e.g., Tables 2-1, 2-2 and Figs. 2-4, 2-7, 2-8 in ten Brink et al., 2007), and various statistics performed on these, we find for the largest SMF scar off of the U.S. East coast, a 15,241 km^2 area, 291 km length, 151 km width, 3,263 m average depth, with a 4,735 m toe depth and a 1,260 m scarp height, yielding a very large volume (for 34 listed slides in their Table 2-2, volume varies between 0.08 and 179 km^3). Furthermore, the same work shows that roughly 50% of the area affected by landslides, and 7 of the 14 landslides in the list that cover areas exceeding 2,000 km^2 are located offshore of Georges Bank and southern New England (a region that covers approximately one third of the length of the study area). Another 24% of the area affected by landslides occurs as two large ones in the Carolina Trough. The remaining 25% of all landslides are spread along the remaining half of the length of the study area. SMFs with volumes

above 100 km^3 (of which there are 4 listed in Table 2-2) can generate runups of more than two meters on nearby coats (e.g., Grilli et al., 2009). The actual magnitude of landslide-generated tsunamis, however, is very site specific and depends on their detailed geometry, location, and volume, as well as on the mode of rupture (Grilli and Watts, 1999, 2005; Watts et al., 2005; Enet and Grilli, 2007; ten Brink et al., 2009a; Geist et al., 2009). Most of these parameters are poorly known or unknown for observed landslide scars.

Hence, for most potential SMFs, both the landslide events themselves and their tsunamigenic potential are a priori unknown. Additionally, landslide triggering by seismic activity is not only a complex phenomenon, but also one that depends on the magnitude of the seismic ground acceleration expected at some distance offshore in the potential slide area (for a given return period), which is poorly known as well over the Atlantic ocean (in part due to the paucity of observed earthquakes). As a partial guidance, for the largest earthquake ever observed along the New England margin, which had a magnitude 7.0 sufficient to trigger a significant SMF (which it did in the 1929 Grand Bank SMF and tsunami, discussed below), ten Brink et al. (2009a) estimate that the return period is between 600 and 3,000 years.

As a result of the lack of data and uncertainties listed above, a comprehensive analysis of SMF tsunami hazard along the U.S. East coast is being conducted in this project, as a separate task, based on Monte Carlo (MC) simulations of slope stability and tsunami generation/runup, similar to the approach detailed in Grilli et al. (2009). Such a MC analysis will provide statistical distributions of potential tsunamigenic SMFs and their parameters, in the region of interest. Once validated using field data (as was done by Grilli et al., 2009 for the region from New Jersey to Cape Cod), such distributions will allow designing a series of relevant SMF sources, which will be used to quantify East coast landslide tsunami hazard by performing numerical simulations of tsunami propagation and coastal impact. In view of this upcoming work, we will limit the present discussion of SMF tsunami hazard to two well-known historical SMF cases, for which landslide tsunamis were either generated, or strongly suspected to have been generated, along the East coast:

1. The first, and only historical SMF tsunami definitely known to have impacted the North American coastline, causing 28 fatalities, occurred on November 18th, 1929, as a result of a submarine landslide caused near the Grand Banks by a large earthquake with $M_w = 7.2$ moment magnitude (to date this still represents the largest earthquake ever recorded in the North American coastal regions of the Atlantic basin). The large slope failure was triggered at the mouth of the Laurentian Channel (Bent, 1994; 1995) on the south coast of Newfoundland, at 44.691°N–56.006°W (Fig. 2), 18 km from the 2 km deep upper continental slope (Fine et al., 2005). The landslide transformed into a turbidity current that flowed over 100 km along the Atlantic floor, at speeds of 60-100 km/h, displacing about 200 km^3 of material. Fine et al. (2005) used a viscous shallow water model to simulate this event, treating the slide as a viscous, incompressible fluid layer. The estimated maximum tsunami wave amplitude was 3-8 m and the maximum runup

observed in Newfoundland was 13 m. While the region affected by such a landslide-generated tsunami was much smaller than that from a typical co-seismic tsunami, such large runups posed a significant locally hazard, as confirmed by the large number of fatalities.
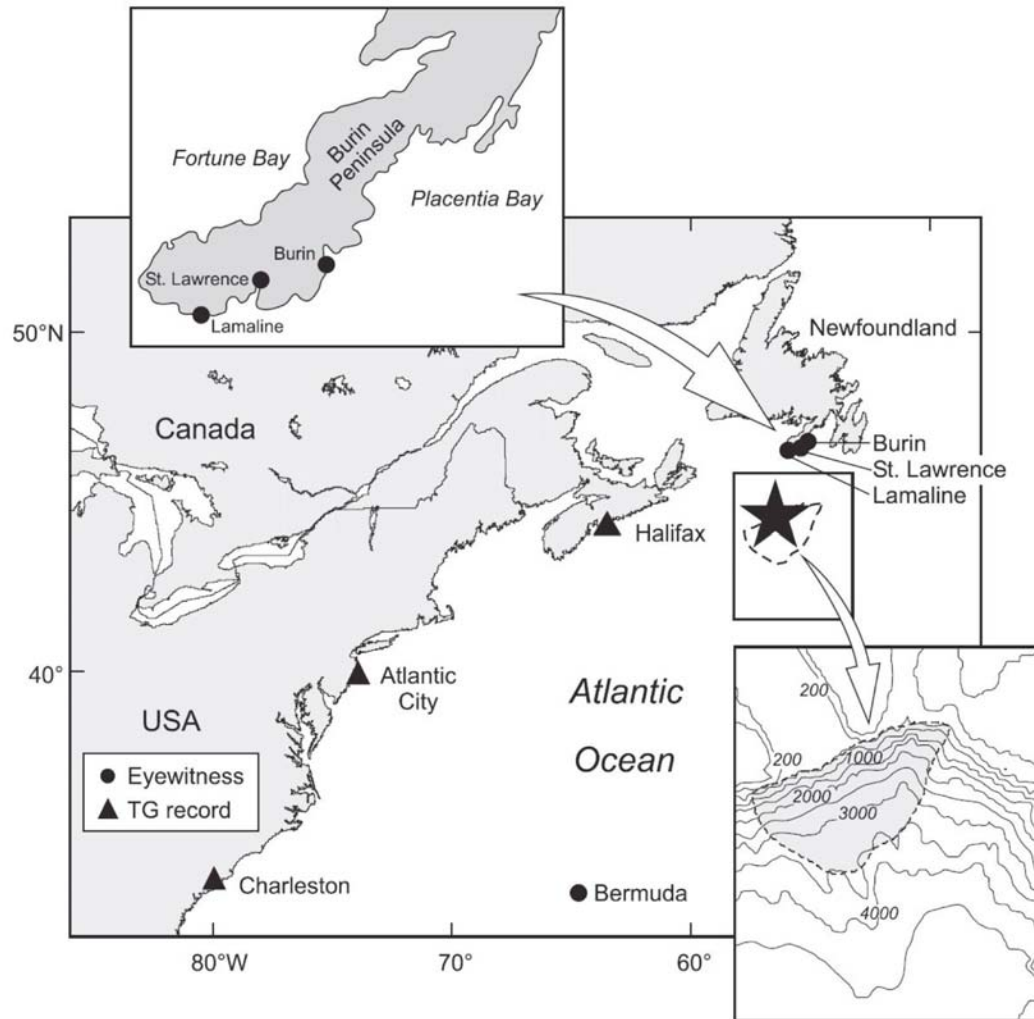

Fig. 2: Location of 1929 Grand Banks SMF, which created a tsunami, noting locations where there were eyewitness or tidal gauge records of the event. The star denotes the earthquake epicenter, and the shaded region (lower right inset) denotes the area of the slide. From Fine et al. (2005).

2. The second, and most notable landslide complex along the U.S. East coast is known as the Currituck landslide, about 100 km off the coast of Virginia and North Carolina (e.g., Fig. 2-9 in ten Brink, 2007). This translational slide is believed to have occurred between 22,500 and 43,300 years ago and was likely a single event caused by an earthquake (Prior et al., 1986). The debris of the slide itself reached as far as 220 km from the shelf edge, and 190 km from the toe of the source area. The down-slope length was about 30 km, the width about 20 km, and the initial thickness was about 250 m (ten Brink et al., 2007, 2008). Volume estimates vary for this event, but the volumes, which were used by ten Brink et al. (2007) for performing simulations of tsunami hazard along the East coast for the

Nuclear Regulatory Commission, are 128 to 165 km^3. Preliminary simulations of a number of Currituck scenarios yield nearshore wave heights of 5-8 m off of the New Jersey Coast.

3. The tsunami generated by this SMF was modeled by Geist et al. (2009), using the dispersive long wave model COULWAVE. Based on Locat et al.'s (2009) mobility analysis, they chose to simulate one of three different landslide volumes: either an event of 108 km^3, 57 km^3, or a composite of the two (165 km^3). For each of the three slide scenarios, they considered different slide durations and bottom friction coefficients. They found a large variation in maximum runup broadside of the Currituck landslide, from 1.20 m to 8.80 m. They found that the most critical parameter for tsunami generation was the landslide volume.

For submarine landslides, previous work has shown that the tsunami generation source can be approximated to a large degree by using simple semi-empirical equations approximating results of numerical model simulations, based on geometric properties of the landslide (such as length, width, thickness, volume, and the slope incline), the bulk density of the material, and some simple hydrodynamic and friction coefficients. This is computationally much faster than using a separate Euler or Navier-Stokes simulation to model landslide physics. This approach has been used to develop semi-empirical landslide tsunami sources based on fully nonlinear 2D and 3D fully nonlinear potential flow simulations of idealized slide or slump cases (Grilli and Watts, 1999, 2001, 2005; Grilli et al., 2002, 2010b; Enet and Grilli, 2003, 2005), and has been successfully applied to perform tsunami case studies (e.g., Watts et al., 2003, 2005; Days et al., 2005; Tappin et al., 2008). An early version of this was described by Watts et al. (2005). See Appendix A for an updated TOPICS implementation of SMF sources.

2.2 Co-seismic tsunamis

The co-seismic bottom displacement resulting from large magnitude earthquakes (i.e., greater than $M = 6.5$ or so), occurring a small depth below the seafloor, may generate significant tsunamis, depending on a variety of geological, geographical, and earthquake parameters. Based on well-known geology and tectonics, co-seismic tsunamis generated by large earthquakes in the North Atlantic would either originate in the Caribbean subduction zone or the Azores-Gibraltar convergence zone (Fig. 1). Each of these has unique characteristics.

2.2.1 Review of literature on Caribbean subduction zone

The Caribbean plate is one of the smallest plates in the world (Figs. 3, 4). It has an approximately rectangular shape and extends from Central America to the Lesser Antilles, and from South Cuba to the South America. The plate pushes its way eastward (at 20-25 mm a year) against the much larger (subducting) North American and South American plates (see, Zahibo et al., 2001, and their Fig. 1 for the geodynamic context of faults in the area; ten Brink, 2007; Jansma, 2008).
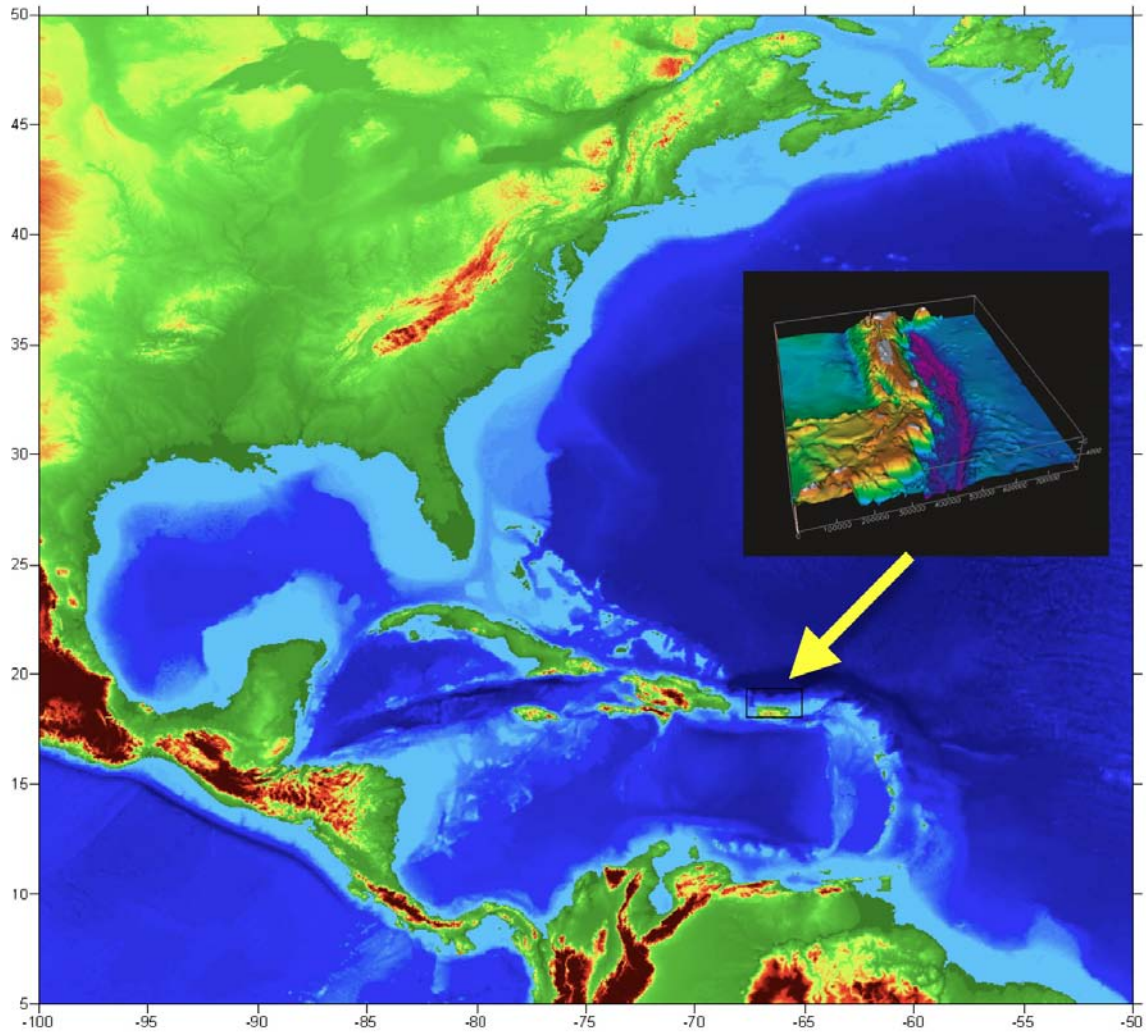
Fig. 3: ETOPO-2 bathymetry (2' accuracy) for the NW Atlantic Ocean basin (axes are in degrees of N Lat. and W Long.). The island of Puerto Rico is marked by a black rectangular box, approximately 204 by 126 km. The sub-figure shows topography and bathymetry in and around Puerto Rico; the 770 km long, 50 km wide, and 7 km deep Puerto Rico Trench (PRT; pink color) is to the north of the island (USGS, 2001).

Its motion with respect to the North American plate causes volcanoes and earthquakes in the region (Zahibo et al., 2003b). The Puerto Rican Trench (PRT; Figs. 3, 4) is at the boundary between these two plates. Figure 3 (sub-figure) shows the topography and bathymetry around the deep PRT, north of the island. The trench is approximately 770 km long and 50 km wide, with a depth reaching over 7,000 m (up to 8,340 m at one location). The northeastern portion of the Caribbean Plate is thus the general tectonic setting for Puerto Rico and the PRT, with the island lying within the East-West trending plate boundary zone (Fig. 4), between the WSW moving North American Plate (to the North and right on sub-figure 3) and the ENE moving Caribbean Plate (left on the sub-figure; Mercado and McCann, 1998).

More specifically, the North American Plate subducts under the Caribbean plate, at a rate that has been estimated from about 20 mm per year (DeMets, 1993) to 37 mm per year (Sykes *et al.*, 1982). As in other recent studies near the PRT area (Zahibo and Pelinovsky, 2001; USGS, 2001; ten Brink and Lian, 2004; tenBrink, 2005, 2007; Jansma, 2008; Grilli et al., 2010a), we assume in the following analyses that there is a predominantly (lateral) strike-slip motion of the Caribbean plate at 20 mm per year with respect to the North American Plate, in the ENE direction, at a 10-20 degree angle with respect to the trench axis.
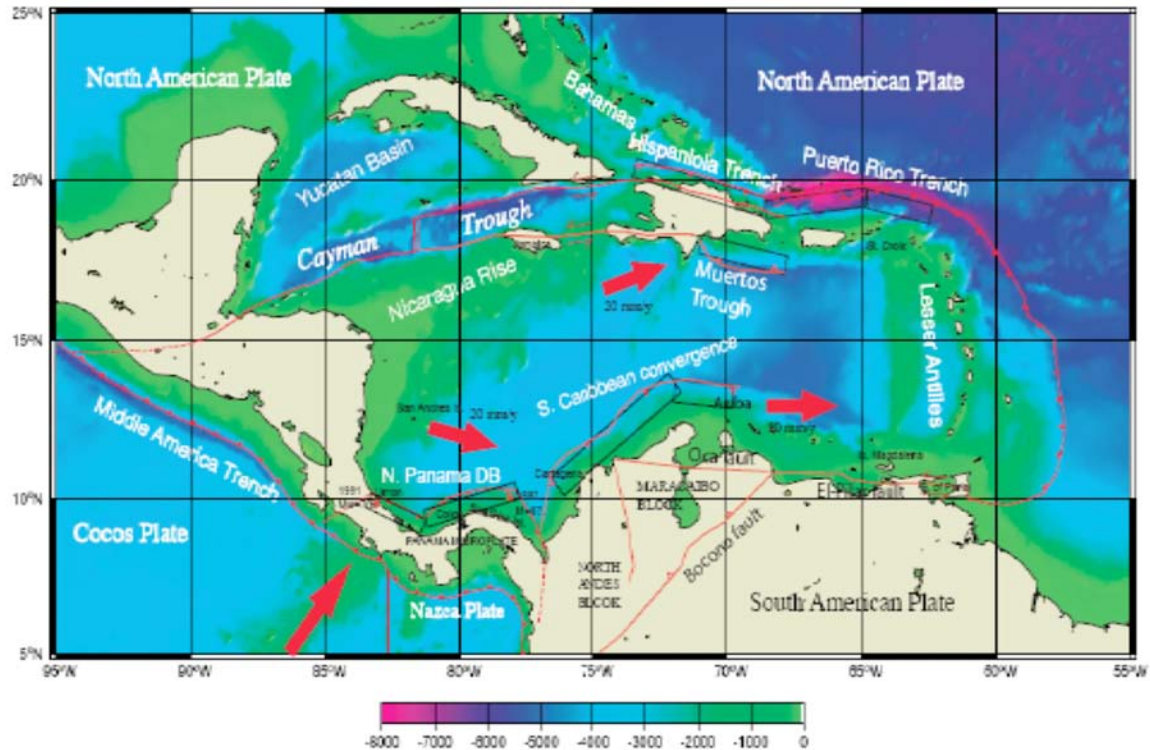

Fig. 4: Boundaries of Caribbean plate with various relevant islands and convergence rates, as well as faults and trenches (from ten Brink, 2007).

Historical analyses of tsunami events in the area overlying the Caribbean plate (including the Caribbean Sea) have catalogued 27 likely candidates (Lander et al., 2002; O'Loughlin et al., 2003; Caribbean Tsunami Hazard, 2006). While some of these candidates have been caused by volcanic eruptions, most have been generated by underwater earthquakes**.** One of the most deadly events among those, the 1918 Puerto Rico tsunami, was generated by a 7.3 magnitude earthquake in the Mona Passage (15 km off the northwest coast of Puerto Rico, approximately 24.2 km west of Punta Higuero) and caused major damage on the West Coast of Puerto Rico (up to 6 m runup and 116 fatalities; Mercado et al., 1998). Mercado and McCann (1998) simulated this event using a linear model for the far-field and a nonlinear model for runup. The oldest recorded tsunami near Puerto Rico occurred in 1867, and was caused by a 7.5 magnitude earthquake in the Anegada Passage (between St. Croix and St. Thomas, US Virgin Islands). The source length was about 10 km, the vertical displacement of the sea floor

was less than 10 m, and the strike of the fault was approximately E-W. This event was modeled by Zahibo et al. (2003a) with the nonlinear shallow water equations. They used different orientations for the tsunami source and investigated the directivity of the wave and distribution of wave height.

While many faults are active in and around the Caribbean, due to its location and predominantly E-W orientation, the PRT would be most likely to cause tsunamis that could reach the U.S. East Coast (see, e.g., Grilli et al., 2010a). As a result of the large component of relative strike-slip motion of the Caribbean plate against the North American plate, frequent small to moderate earthquakes occur in the PRT region (see, Zahibo et al., 2003, their Fig. 1, and ten Brink, 2005, for historical maps of seismicity in the larger Caribbean Sea area), for which ten Brink (2005) mapped the depth and intensity (for $M > 2.5$); earthquake locations are clearly aligned with the boundary of the subducting plates. By contrast, the same analysis only identifies 6 large historical events of magnitude 7 or greater (a typical threshold for potentially large tsunami-genesis; Table 1), for the past 220 years in or near the PRT. Among these, two events occurred with (estimated) magnitude greater than 8, and four reportedly generated a tsunami, with three causing a 5-7 m runup on Puerto Rico (cases 3-5; USGS, 2001; Zahibo et al., 2001, 2003; Lander et al., 2002). For completeness, it was also reported by Dawicki (2005) that twelve earthquakes of magnitude 7 or greater occurred near Puerto Rico in the past 500 y., but no additional tsunami records, other than those presented in Table 1, were given.

Earthquake location	Date	Magnitude	Tsunami	Casualties	Runup (m)
1. Hispaniola	1953	6.9			
2. Mona Passage	1946	7.5	Yes	40	
3. Hispaniola	1946	8.1	Yes	1,800	5
4. Mona Passage	1918	7.3	Yes	91–116	6
5. Anegada Trough	1867	7.5	Yes	?	7
6. Puerto Rico Trench	1787	8.1			

Table 1 : Largest historical seismic events around Puerto Rico (USGS, 2001).

The catastrophic 7.0 magnitude (shallow) earthquake that hit Haiti (on the island of Hispaniola just West of Puerto Rico; Fig. 4) on Jan. 12th, 2010, heavily damaging Port-au-Prince and killing over 217,000 people in the process, recently reminded us of this potential for large earthquakes in the area. While this earthquake was mostly land-based and only generated a small tsunami, a large ocean-based earthquake in the PRT could generate a significant tsunami that might have catastrophic effects in the near-field on the lower lying coastal areas of the Puerto Rico North Shore (e.g., San Juan), as well as induce significant far-field effects on distant shores, including the US East Coast (see, e.g., Grilli et al., 2010a). Mercado et al. are conducting NTHMP funded tsunami simulation work to create tsunami inundation maps along the Puerto Rico shore. Hence, here, we focus on future events in the PRT (and nearby faults) whose far-field impact could affect or govern the East coast tsunami hazard. Because of the lack of large earthquakes in the PRT in the past 200 years (Table 1) a large and potentially

tsunamigenic earthquake should be expected in the near future. In fact, tenBrink and Lian's (2004) recent survey of the PRT uncovered evidence of current seismic activity and internal stress build-up in the subduction zone near the PRT, which supports the "impending" occurrence of a potentially large earthquake in the trench, and justifies the urgency for estimating tsunami hazard in the region and in the far-field, as a result of it.

Accordingly, there has been substantial recent research into defining reasonable earthquake scenarios to perform simulations of tsunami generation and estimate both the resulting near-field and far-field tsunami hazard (e.g., Knight, 2006). Following Grilli et al. (2010a), we detail below the rationale for developing such scenarios, which include both estimated earthquake parameters and return period.

Although a rigorous analysis of earthquake and tsunami return periods would be difficult to perform, due to the paucity of observations of large seismic events and tsunamis in the region (only one historical event, case 6 in Table 1, is specifically sited in the PRT), it appears from data in Table 1 that there were 3 large tsunamigenic events affecting Puerto Rico during an 80 year period and 5 large earthquakes during a 160 year period in the Puerto Rico area, two of those with magnitude greater than 8. Hence, as a first approximation, one can associate a magnitude 7.5-8.1 seismic event in the area around Puerto Rico with a 30 to 80 year return period. Similarly, Dawicki's (2005) data would yield an average 42 year return period, for events of magnitude 7 or greater, which is consistent with the latter data. Longer period events have not been observed, but based on estimated plates' subduction rate and approximate maximum length and width of the PRT area that could move during a future large scale event, one could try and estimate the magnitude of extreme seismic events in the trench, as a function of their return period. This is discussed below.

To prepare for the impact on the U.S. East coast from future major tsunamis in the Caribbean region, Knight (2006) developed a first-order estimate of the most extreme earthquake that could occur in the PRT, and assessed the resulting potential tsunami hazard (mostly for the Caribbean islands and lower East coast). Although Knight's was not an extensive analysis, it showed that only the largest earthquakes from the Caribbean subduction zone should be of concern for the U.S. East coast, and the focus of future work should be on sources originating in the PRT. More specifically, in his work, Knight assumed a simple homogenous source model (i.e., without considering effects of shores, small islands and archipelagos), covering a 600 km by 150 km area of the Puerto Rico trench (i.e., nearly the full E-W extension of the PRT by three times its actual width), with a fault plane orientation based on the PRT geology (angles are given in a following section). This extreme source corresponded to a magnitude 9.1 earthquake, which using Okada's (1985) method yields an average slip of $\bar{\Delta} = 11.9$ m (and maximum slip of $\Delta = 19$ m; see details of our slightly modified version of the method in Appendix A). Based on the estimated 20 mm per year subduction rate in the region, this average slip would yield a long return period earthquake of 600 year or so. Now, if the two largest historical events of magnitude 8.1 listed in Table 1 had affected the same (entire) area of the PRT, one could estimate their return period by prorating average slip to the released energy, as compared to the 9.1 event (note, under Okada's (1985) method assumptions, total energy

released by an earthquake is proportional to the assumed surface area and average slip; see appendix A for details). This can be done using Hanks and Kanamori's (1979) relationship between energy M_o [J] released by an earthquake and its moment magnitude defined as: $M_w = \log M_o/1.5 - 10.7$ (where $1.51 = \log 32.36$), which for a very significant $M_w=8.81$ event yields an average slip: $\overline{\Delta}_{8.1} = \overline{\Delta}_{9.1} / 32.36^{(9.1-8.1)} = 0.37$ m. Based on the estimated subduction rate in the PRT, this would only represent a 20 year or so return event, while historical data points to a longer 30-80 year return period. This implies, as could be expected, that in such smaller but still significant events only a fraction of the length of the PRT was likely mobilized by the earthquake. For instance, for the same M_w = 8.1 event, due to the proportionality of released energy to slip and surface area, reducing the affected length of PRT to 300 km would increase average slip to 0.74 m and the estimated return period to 40 years or so. Note, this would also have the effect of proportionally increasing the initial tsunami source and further concentrating its effects on lands and islands closest to the earthquake area, around the PRT. However, since no or few observations were made for these historical events, it is nearly impossible to further constrain the tsunami source based on hydrodynamic observations (as, e.g., was successfully done for the widely observed 2004 Indian Ocean Tsunami; see, e.g., Grilli et al., 2007; Ioualalen et al., 2007).

Grilli et al. (2006, 2010a) performed numerical simulations of near- and far-field tsunami impact on the basis of Knight's extreme "600 year" 9.1 magnitude source (Fig. 5). Additionally, as it was desirable to estimate the likely maximum event that could occur in the PRT in the near future, Grilli et al. (2010a) developed a 200+ year return period source, affecting the entire area (600 x 150 km) of the PRT, based on accumulated potential slip in the trench since the last known event that significantly affected it in 1787, i.e., 223 years ago. This represents a $\overline{\Delta} = 4.46$ m average slip and the resulting source for this event has a 8.7 magnitude and maximum slip $\Delta_{8.7} = 4.72$ m.

Finally, for completeness, other work focused on the Caribbean Sea and Lesser Antilles, S and SE of Puerto Rico, where local earthquakes and volcanic eruption could (and have) caused regional tsunamis. These however, would be too small and/or somewhat blocked by Puerto Rico, to have a significant impact on the U.S. East Coast. Thus, Zahibo and Pelinovsky (2001) evaluated the tsunami risk in the Caribbean Sea area, which includes both earthquakes and volcanoes. They find that co-seismic tsunamis would be likely larger in the region than landslide or volcanic tsunamis. Zahibo et al. (2003b), using a model based on the nonlinear shallow water equation, simulated potential tsunamis in the Caribbean Sea and their impact on various coasts. Based on historical data, they mentioned the Caribbean crossing time would be about 3.2 hrs for lateral transfer and 1.2 hrs for meridional crossing. Nikolkina et al. (2010) analyzed historical tsunami data for the region around Guadeloupe, and found that the French West Indies subduction zone has the potential for tsunamigenic earthquakes of up to $M_w = 8.3$. They also reported reliable and validated data regarding historical events in the Caribbean Sea, indicating that the return period for tsunamis in the Caribbean is about 3 years (although many are only local events, and not all of the historical records are definitive).
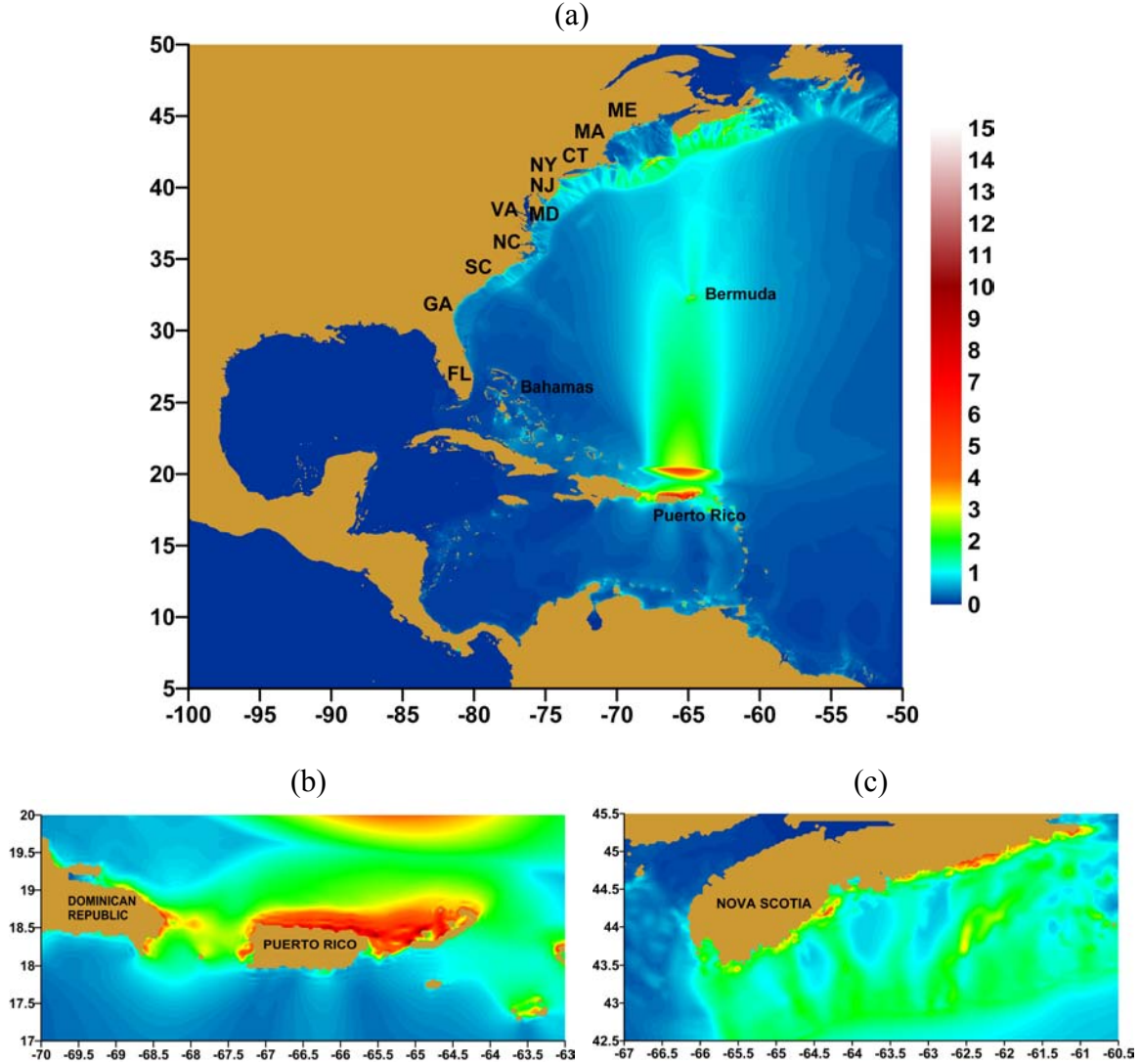
(a)

(b)   (c)

Fig. 5: Grilli et al.'s (2010a) FUNWAVE simulations over a 2'x2' grid for a 9.1 co-seismic tsunami source in PRT (axes are in degrees of N Lat. and W Long.): (a-c) Maximum surface elevations (color scale in meter) at anytime during computations. Zoom near and around (b): Puerto Rico; (c): Nova Scotia.

Based on the above, for simulating the far field effect on the U.S. east coast of large co-seismic tsunamis initiated in the PRT, we propose to use Grilli et al.'s (2010a) extreme (600 year) $M_w = 9.1$ source, affecting the entire PRT 600 x 150 km area. Fig. 5 shows Grilli et al.'s (2010a) FUNWAVE results for the maximum tsunami elevation caused by this source, in both the near- and far-field, in a coarse 2' x 2' Atlantic basin grid, using ETOPO-2 ocean bathymetry merged with the NGDC 3" Coastal Relief Model (Divins and Metzger, 2008) below 19 deg. N, North of Puerto Rico. Fig. 6 shows an example of coastal impact computed for this event, in a finer 15" x 15" regional nested grid, along the U.S. East coast from New Jersey to Cape Cod (MA). Additionally, we will use a series of 200 year $M_w = 8.7$ sources, the first one being similar to Grilli et al.'s (2010a) and others only affecting a reduced length of the PRT of 300-400 km, with the source epicenter moved among a few locations, from E-W (e.g., 4).

Quantities	9.1 source	8.7 source
Epicenter	19.5° N 66° W	19.5° N 66° W
Strike (degrees)	92	92
Dip (degrees)	15	15
Rake (degrees)	50	50
Maximum slip (m)	19.0	4.72
Fault plane depth (km)	40	40
Length (km)	600	600

Table 2: Okada's parameters for 9.1 and 8.7 sources for Grilli et al.'s (2010a) FUNWAVE simulations.

(a)

(b)
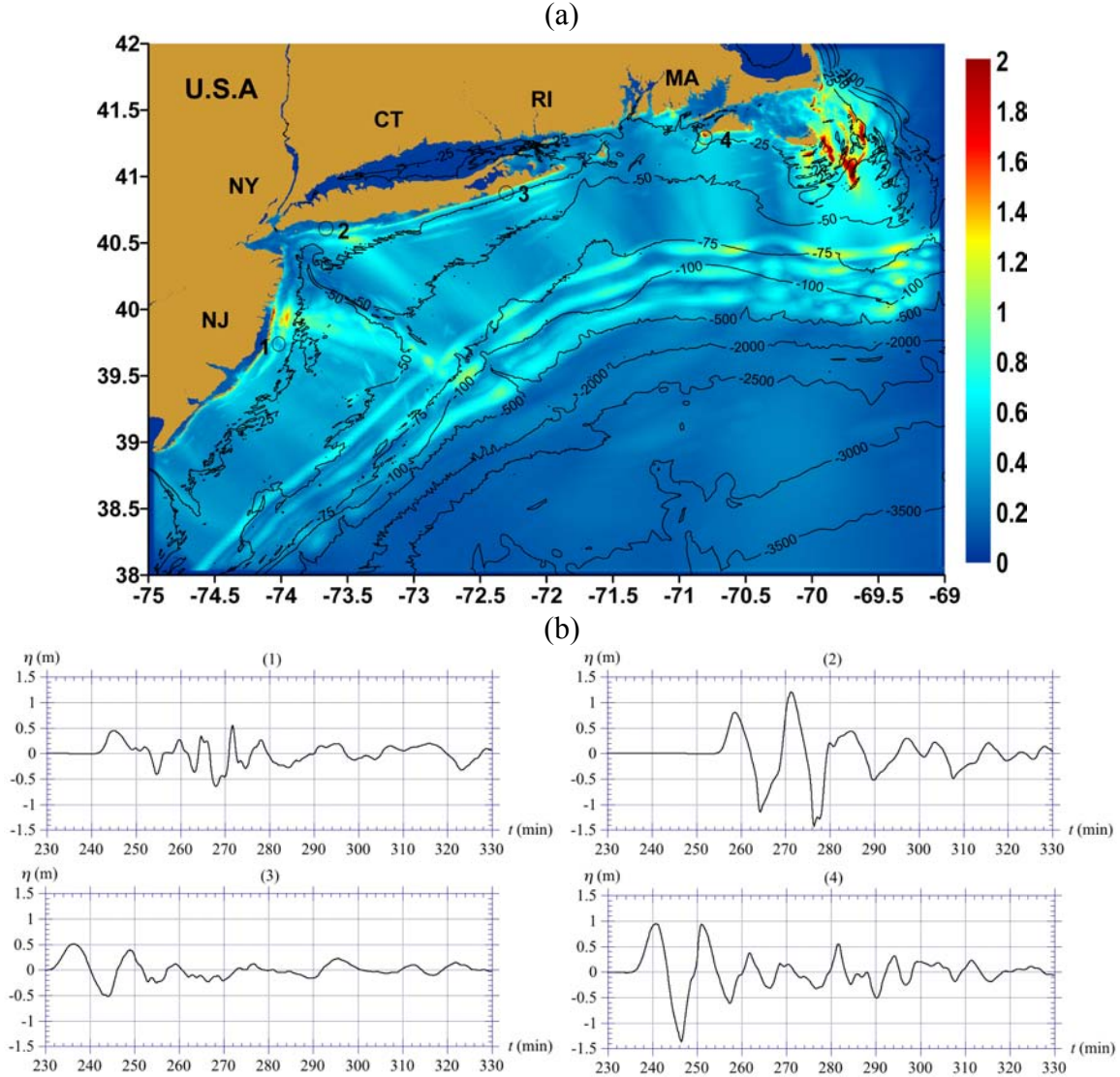
Fig. 6: Same case as Fig. 5. (a) Maximum tsunami elevation for the New Jersey, Long Island, Rhode Island and Cape Cod coastal areas, in a nested 15" regional grid (initialized with Fig. 5 results; color scale in meter; axes are in degrees of N Lat. and W Long.); (b) time series of tsunami arrival at locations 1-4 (numerical gages) marked as symbols (o) in Fig. (a), with depth 14.4, 3.2, 18.1 and 14.8 m, respectively; times correspond to the start of the tsunami event in the PRT.

Okada's parameters used for generating these sources with TOPICS are given in Table 2. Note, these two sources are consistent with ten Brink and Lin's work (2004), who stated that the worst-case scenario for an earthquake rupture along the PRT is a single 675 km long rupture, between 68°W and 62°W. As an example, for a 10 m average slip and shear modulus $\mu = 3 \times 10^{10}$ Pa, the rupture area 675 by 102 km, the moment is $M_w = 8.9$, which is in the proposed range for our work.

2.2.2 NOAA Forecast Source Database for Caribbean subduction zone

      The NOAA Center for Tsunami Research (NCTR) has produced a series of model runs corresponding to various faults around the world (Gica et al., 2008). For the Caribbean subduction zone, this consists in a series of 214 different sources, with 1 m average slip, a fault length of 100 km, width of 50 km, and generating an energy corresponding to a $M_w = 7.5$ moment magnitude earthquake. Based on available data about various faults, reasonable estimates of the epicenter longitude and latitude, strike angle, dip angle, and depth of the unit sources are provided. Based on NOAA's unit source simulations, maps of maximum tsunami elevations can be produced, such as Fig. 7 for one of these unit sources. We see that while overall far-field impact depicted in Fig. 7 follows a pattern similar to that in Fig. 5a, the maximum elevation is much reduced (by about a factor 100 in the U.S. upper East coast), consistent with the much reduced energy in a 7.5 source, as compared to a 9.1 source (factor of 110 based on Kanamori's relationship). Note, the concentration of wave energy in Fig. 7 off of South Carolina, which is also present in a large number of NOAA's unit source simulations and is likely caused by wave focusing on Blake ridge.

      While the work of Gica et al. (2008) was primarily aimed at producing tsunami elevation to be used in the Caribbean basin for the Short-term Inundation Forecast for Tsunamis (SIFT) system (an operational tool for rapid forecasts of tsunami impact), rather than creating a worse case scenario in the far field, such results can be used in the present work to better understand both the types of impacts from tsunamigenic earthquakes in the area, as well as providing a rough estimate of expected FUNWAVE results (as shown before) for such sources. One additional result in Gica et al.'s (2008) work, which is important for our simulations, is their sensitivity analysis of tsunami generation to earthquake source parameters. They found that variations in earthquake epicenter location and magnitude were relatively more important for tsunami generation than changes in dip angle, rake angle, average slip value, and fault area. Hence, to a first order, tsunami generation depends more on the average location where the total seismic energy is released and less on the details of the geological parameters affecting this release. This should be even truer in the far-field, where small differences in tsunami waves near the source area should be attenuated.
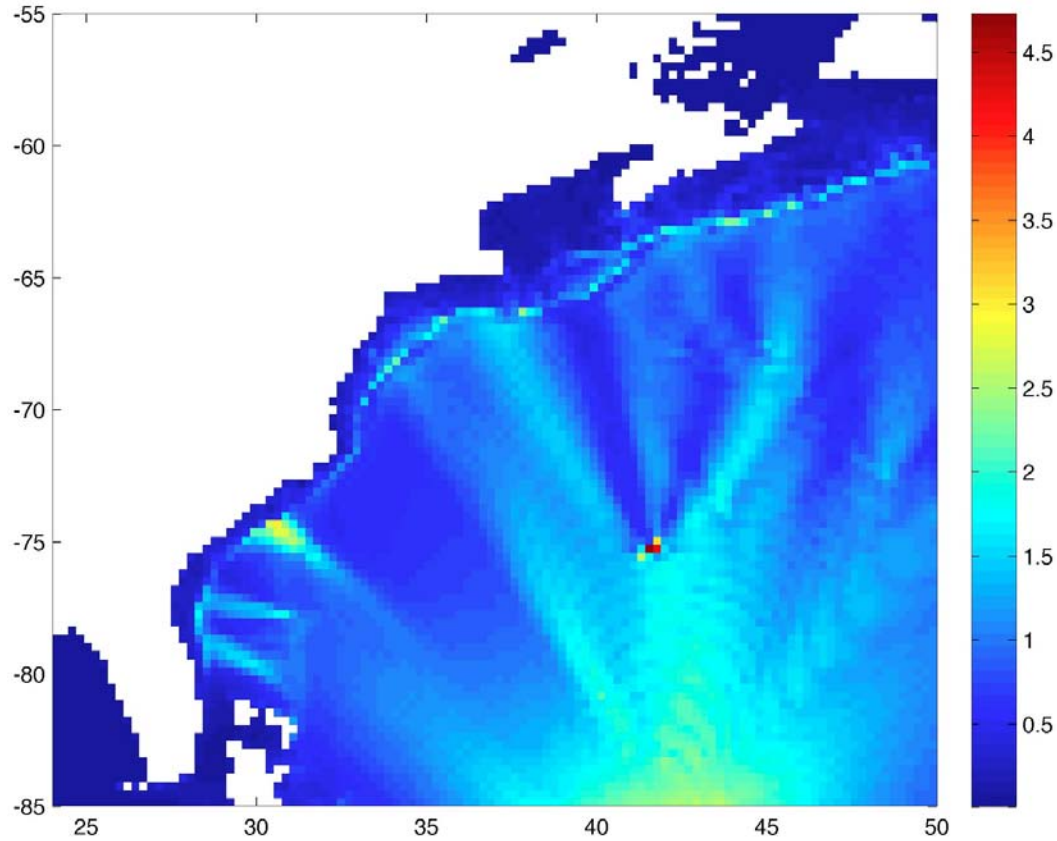
Fig. 7: Maximum wave height (cm) in NW Atlantic basin, off of the U.S (N Lat-W Long. coordinates). East coast as modeled for NOAA Forecast Source Database unit slip surce case *atszb49* (centered at 19.3859° N 64.7814° W, with a strike angle of 94.34°, a dip angle of 20.00°, and a depth of 5.00 km).

2.2.3 Azores-Gibraltar convergence zone

The other main source of co-seismic tsunamis in the Atlantic basin is the Azores-Gibraltar convergence zone (see Fig. 8 and bathymetry in Fig. 9). There are several potentially active faults in this convergence zone, including the Gorringe Bank Fault, the Marque de Pombal Fault, the St. Vincente Fault, and the Horseshoe Fault (Fig. 8). Collectively these faults are considered to be the source of some of the largest historical earthquakes and tsunamis in the Atlantic ocean, including the devastating Lisbon 1755 $M_w = 8.5$-9 magnitude earthquake and tsunami, which caused up to 100,000 deaths and generated 5-10 m initial surface elevations (Baptista et al., 1998a,b; Gutscher et al., 2006), yielding some significant tsunami runup as far as North America. In the far field, Lockridge et al. (2002) reported on the 1755 tsunami runup in the Caribbean. Antigua, Saba, and St. Martin at the northeast corner of the Caribbean Sea had the highest runup, but flooding was also reported from Santiago de Cuba and Samana Bay, Dominican Republic, in the North to Barbados in the south, as well as north of St. Johns, Newfoundland, but there are no reports of flooding anywhere else between Cuba and Newfoundland, despite the presence at that time of population centers in low-lying areas

of the eastern U.S. and Canada (ten Brink, 2007, 2008). As the current NOAA Forecast Source Database does not include potential distant sources in the Azores-Gibraltar convergence zone, we will estimate their parameters based on the existing literature.
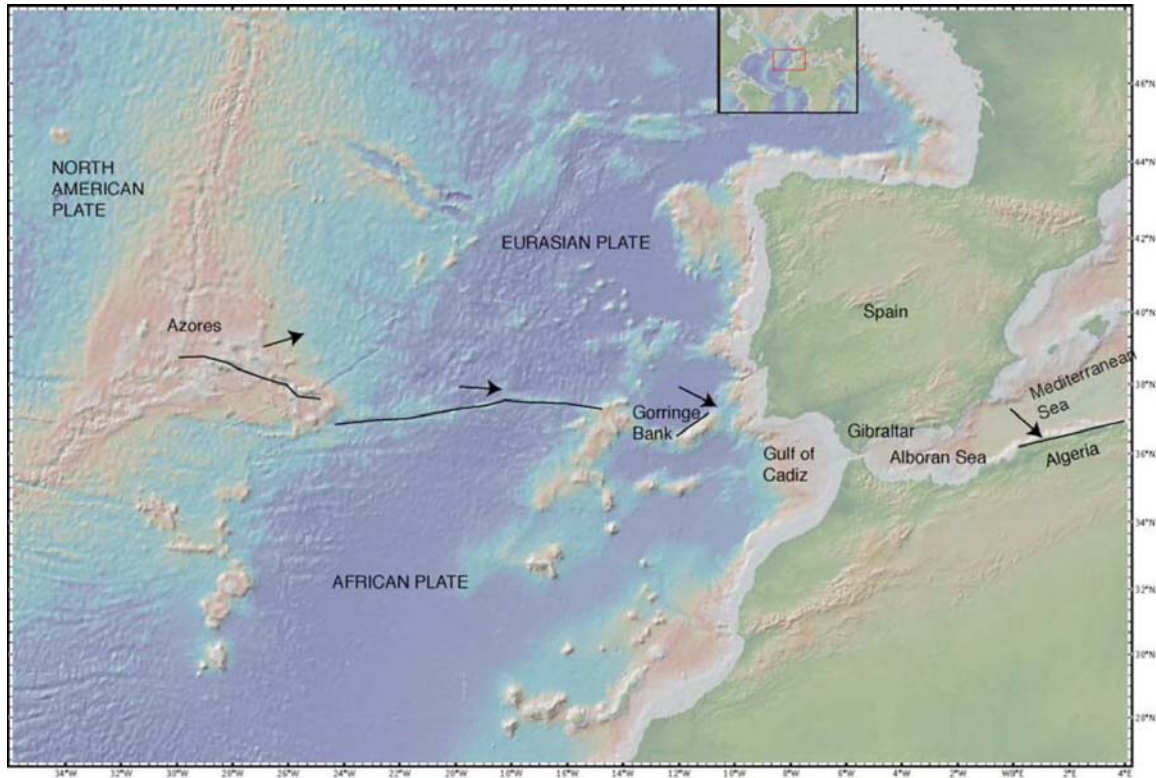

Fig. 8: Geodynamics of and boundaries between the African and Eurasian plates, near the Azores-Gibraltar convergence zone. The relative motion of the Eurasian plate relative to the African plate is 4 mm/year (from ten Brink, 2007). Some of the major potentially active faults are shown on the figure.

The boundary between the large African and Eurasian plates extends from the Azores Triple Junction in the west to the area SW of the Iberian Peninsula. The relative plate motion is strike-slip, with a slight divergence at the western end near the Azores and convergence near its eastern end, a modest 4 mm/year (Fig. 8, e.g., Argus *et al.*, 1989). The juxtaposition of two old and dense plates along the eastern end does not allow for subduction to develop (e.g., Grimison and Chen, 1986). Instead, a zone of diffuse compressive deformation has developed, with Gorringe Bank and other lesser banks and seamounts, being separated by abyssal plains of great depth (Fig. 9; Hayward *et al.*, 1999). Ten Brink et al. (2007, 2008) report that four large tsunamigenic earthquakes have occurred in the Atlantic Ocean west of Gibraltar in the last 300 years: (i) the 1722 (Baptista and Lemos, 2000); (ii) the $M_w = 8.5$-9 Lisbon 1755 (e.g., Johnston, 1996; Baptista et al., 1998a,b; Gutscher et al., 2006; Grandin et al., 2007); (iii) the 1761 (Baptista *et al.*, 1998); and (iv) the $M_w = 7.8$ 1969 (Johnston, 1996) earthquakes. However, there is no simple tectonic model for this area that explains the generation of these earthquakes. While it is not clear which faults are presently active in the region, the

fact that an earthquake (and tsunami) as large as that of 1755 could be generated in this area, shows that this event deserves further analysis in the context of the present study.
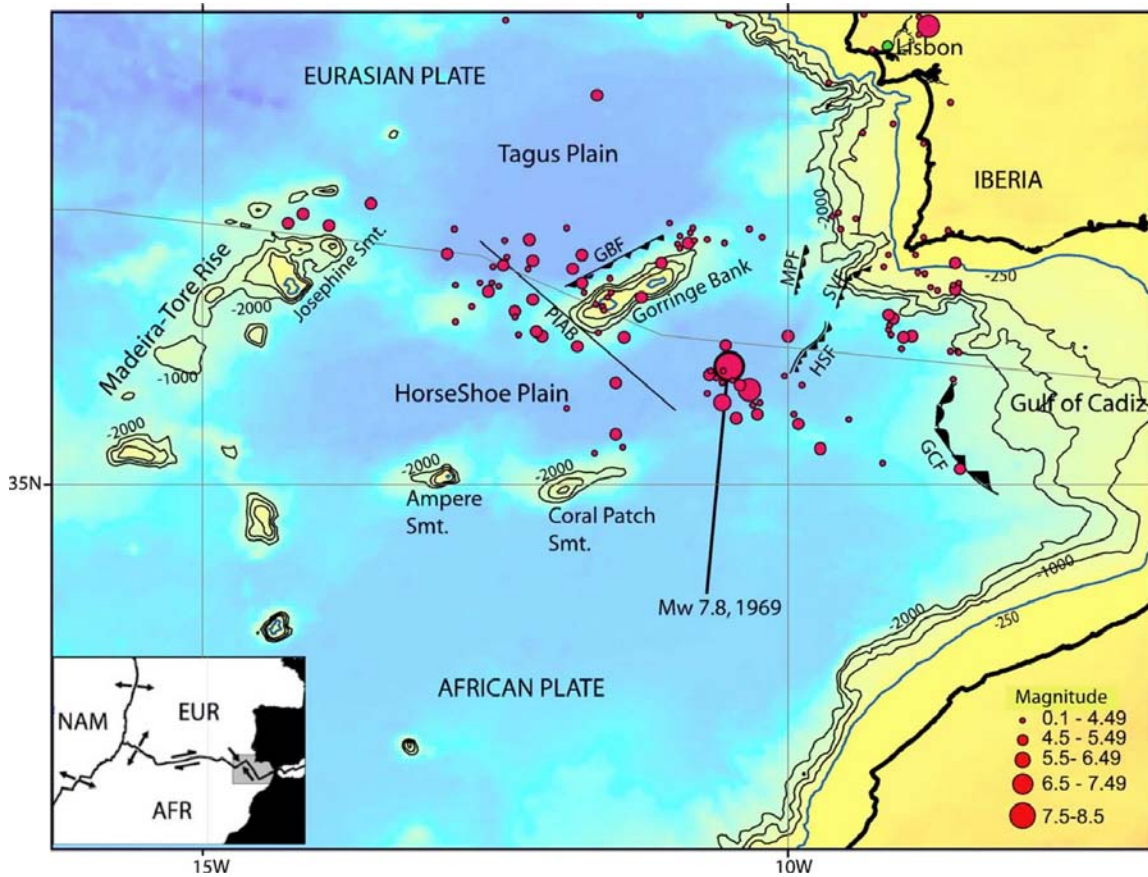

Fig. 9: Area around the Azores-Gibraltar convergence zone, including locations of past earthquake epicenters, as well as proposed faults from previous studies (GBF – Gorringe Bank Fault; MPF – Marques de Pombal Fault; SVF – St. Vincente Fault; HSF – Horseshoe Fault; GCF – Gulf of Cadiz Fault), and the Paleo Iberia – Africa Plate boundary. From Barkan et al. (2009).

As indicated, there is no clear consensus on the location and parameters of he Lisbon 1755 earthquake and tsunami source. Johnston (1996) assumed that Gorringe Bank, which is the major morphologic feature off of Lisbon, rising from a depth of 4,000 m to 25 m (Figs. 8, 9), was the source of the November 1, 1755 Lisbon Earthquake. The same work concluded that the $M_w = 7.9$ 1969 earthquake occurred on a fault parallel to the Gorringe escarpment, but 90 km to the SE. The strike directions of the escarpment and the earthquake were 45°-50° and slip of the 1969 earthquake was to the NW. Johnston proposed the following parameters for the 1755 Lisbon earthquake source: 200 km length, 80 km width, 40° dip angle, 62° strike angle, 332° slip angle, 12 m average slip (the rock density was further selected as 3,330 kg/m^3 with a shear modulus $\mu = 6.5$ x 10^{11} dyne/cm^2). By contrast, Gracia et al. (2003) proposed that the 1755 Lisbon earthquake occurred on two other thrust faults (Marques de Pombal fault and Horseshoe-San Vincente fault). These faults have an average strike of 20° and their suggested slip direction was to the NW. Gutscher et al. (2006) attribute the 1755 earthquake to thrusting

19

and subduction of the Eastern Atlantic under the Alboran Sea. The average dimensions of their NS oriented fault plane are: 180 km length and 210 km width. Moment magnitudes were calculated for two average co-seismic slips of 20 and 10 m using $\mu = 3 \times 10^{10}$ Pa, yielding $M_w = 8.8$ and 8.64, respectively. According to the authors, such an earthquake would have a 1,000-2,000 year return period.

The Lisbon 1755 earthquake was highly tsunamigenic, and its far-field tsunami impact (including on the North American coast) was modeled by Baptista et al. (1998a,b), Mader (2001) and Barkan et al. (2009). Such studies can be useful not just for understanding tsunami hazard itself, but also for constraining the tsunami earthquake source. Thus, Baptista et al. (1998a,b) performed inverse ray tracing using near-field coastal tsunami observations, yielding an optimal location for the 1755 earthquake source as a composite rupture along the SW Iberian coast, with strikes of 160° and 135°. Barkan et al. (2009), after simulating several possible sources, suggested that the 1755 earthquake was generated in the Horseshoe Plain area. It should be noted that other sources selected in the same area, in the same study, while not as closely matching the historical records of the generated tsunami, were shown to cause a tsunami that could reach the coast of Florida. According to ten Brink (2007), if one assumes that the highest observed runup was in the direction of fault slip, then the slip azimuth from the Gulf of Cadiz to Saba is 263°, and if the fault strike is perpendicular to slip then the fault strike was 173°. This fault strike is compatible with the fault strikes proposed by Baptista *et al.* (1998a,b) and Gutscher *et al.* (2006) and is incompatible with the sources proposed at Gorringe Bank (Johnston, 1996).

Fault parameters	Gulf of Cadiz	Step-over	Marques de Pombal
Epicenter	35.441°N 8.614°W	36.7310°N 9.2155°W	37.410°N 9.647°W
Strike (degrees)	343	285	330
Dip (degrees)	49.4	24.8	26.1
Rake (degrees)	5	25	25
Max. slip (m)	20	15	15
Fault depth (km)	10.0	12.7	11.0
Length (km)	180	130	100
Width (km)	210	60	50
Delay (s)	0.0	51.67	89.67

Table 3: Okada's parameters for Lisbon 1755 earthquake faults used by Watts (2006).

A similar case study of the 1755 tsunami was conducted by Watts (2006), with the goal of reproducing the near-field observations. Based on ground motion and geological interpretation by Risk Management Solutions, Inc., three different tsunami sources were identified (Table 3; note the shear modulus used was never specified), which were used to initialize the tsunami propagation model FUNWAVE, using TOPICS. This preliminary work was able to establish that the fault rupture most likely happened from the south to the north. From his simulated results, Watts was able to get

good agreement with observed runup at most locations. The most notable difference was that low runup was predicted at some locations, as compared with observations, suggesting that perhaps a local landslide tsunami may have been triggered by the earthquake as well

2.3 Cumbre Vieja Volcano flank collapse

Another distant tsunami source that could affect the U.S. East coast would be caused by the potential lateral collapse of the Cumbre Vieja Volcano (CVV) on La Palma, in the Canary Islands (Fig. 10). Since the pioneering, but controversial, work of Ward and Day (2001), the potential CVV flank collapse has been the object of numerous tsunami hazard studies, in particular, regarding the U.S. East coast. Indeed, Ward and Day assumed an extreme scenario for the western flank collapse, involving a volume of about 500 km^3 (with a 15-20 km width and a 15-25 km length) and found that such a mass, sliding at speeds up to 100 m/s into the deep ocean, would generate initial waves with height in excess of 1 km. Such large waves would propagate across the Atlantic Ocean and severely impact distant shores. Based on their highly idealized source and calculations (using a superposition of linear waves), Ward and Day concluded that far field tsunami waves would cause a 10 to 25 meter runup along the US East coast (from North to South).

Fig. 10: Cumbre Vieja volcano (CVV) in La Palma (Canary Islands).

Ward and Day's catastrophic subaerial landslide scenario and wave modeling approach were severely criticized in later work (e.g., Mader, 2001; or Pararas-Carayannis, 2002; Wynn and Masson, 2003). Mader (2001), for instance, performed simulations of the tsunami that would be produced by the same extreme 500 km^3 scenario, using the Navier-Stokes (NS) wave model SWAN, and found an order of magnitude smaller waves in the far field than Ward and Day's. Mader's simulations indicated that up to 3 m high tsunami waves could reach the U.S. East coast for such an event. A more rigorous modeling of the slide event and wave propagation was done by Gisler et al. (2006) and Løvholt *et al.* (2008), on the basis of a multi-material NS model for the slide and a dispersive Boussinesq equation model for tsunami propagation, which

confirmed earlier criticism. Using a smaller 375 km^3 scenario, these simulations predicted significant wave dispersion, and amplitude decay proportional to the inverse of the distance to the source. In the far-field, they predicted up to a 0.8 m wave amplitude in Florida (i.e., a 1.6 m height), but other areas of the U.S. East Coast could be more impacted (this is somewhat consistent with Mader's predictions). Note, for completeness, that Grilli et al. (2006) and Pérignon (2006) had also performed earlier simulations of CVV flank collapse scenarios, using a dispersive Boussinesq model (FUNWAVE) to simulate tsunami propagation, but a simpler semi-empirical subaerial landslide tsunami source (Walder *et al.*, 2003). The proprietary nature of this work, however, had prevented its publication until recently.

Geological studies were also motivated by Ward and Day's (2001) work. Thus, Masson et al. (2002, 2006) found evidences of past large paleo-submarine landslides of volume 50-500 km^3, around the Canary Islands, at least demonstrating that such events were not purely speculative. They found an average recurrence period for 15 such events of O(100,000) years. However, turbidite deposits indicate that such large slides may have occurred in a retrogressive way, which would have reduced their tsunamigenic potential. McMurtry et al. (2007) found an abnormally high elevation of ancient marine sediment deposits in the path of Ward and Day's and others' calculated waves, which would be consistent with a large tsunami. Hence, if on the one hand the alarming work of Ward and Day (2001) may be subject to criticisms as documented in subsequent work reviewed above, on the other hand, the lack of knowledge regarding such extreme natural hazards and related tsunami phenomena, warrants further analysis in the context of the present work.

Hence, in a separate task of this NHTMP project, we perform new simulations of CVV flank collapse scenarios, using the incompressible multi-fluid 3D-NS Volume Of Fluid (VOF) model (referred to as THETIS; e.g., Abadie et al., 2010). THETIS' output is used as an initial condition for the (fully nonlinear and dispersive) Boussinesq model FUNWAVE, in which we perform simulations of transoceanic tsunami propagation and impact on the U.S. East coast, in a series of nested model grids. Regarding CVV landslide scenarios, following the initial work of Abadie et al. (2008), these are based on new slope stability analyzes of the CVV western flank, conducted as part of the European research project TRANSFER (Fabre et al., in revision). In these studies, potential failure surfaces are inferred from field data, laboratory tests, and slope stability analyses performed in a series of 2D vertical slices (in the volcano western flank), using two different numerical models, based on a Mohr-Coulomb failure criterion. The likeliest failure surface is identified by gradually decreasing material property values (thus mimicking hydrothermal alteration of the CVV flank). A global shear zone, more or less parallel to the topography and dipping 24° westward, was thus identified, based on global plastic indicators and areas of maximum shear strain. On this basis, a 2D slide cross-section was finally defined, which allows calculating slide volume based on field data (width and length of semi-elliptic shape). Doing so, Fabre et al. estimated potential CVV landslide volumes ranging between 38 and 68 km^3, depending on the hypotheses made on the lateral extent of any given failure. These values, which are much smaller than the 500 km^3 volume proposed by Ward and Day (2001) (and later used in Gisler et al. 2006, and

Løvholt et al. 2008), appear to be more reasonable in view of the size of deep water deposits identified at the toe of the volcano, possibly corresponding to the CVV last massive flank collapse (about 300,000 years ago).

In summary, slide volumes of 38 to 68 km^{3}will be used in the present NTHMP CVV modeling studies, but the 500 km^3 scenario will still be simulated to compare our results with Løvholt et al.'s (2008). Note, however, that the high safety factors found in Fabre et al.'s analyses indicate that the CVV western flank is rather stable under present conditions. Large seismicity and/or a volcanic eruption could nevertheless provide additional destabilizing forces that were not included in their analyses.

3. INITIAL SOURCE DEFINITIONS AND TSUNAMI SIMULATIONS

3.1 Modeling methodology

Tsunami propagation simulations will be performed for a series of tsunami sources, using the Boussinesq model FUNWAVE, either in its original fully nonlinear Cartesian implementation, for the finer regional nearshore grids (see Wei et al., 1995; Wei and Kirby, 1995), or in its more recent weakly nonlinear spherical coordinates implementation, for the ocean basin scale grids (Kirby et al., 2009). The fully nonlinear model is based on a second-order series expansion of the vertical variation in velocity potential. Unlike the Nonlinear Shallow Water (NSW) equations, traditionally used for studying tsunami propagation and coastal impact, the Boussinesq approach includes dispersive effects, which may be significant for landslide tsunami sources and affect tsunami propagation and runup through wave-wave interactions. To simulate both wave breaking and inundation over dry land, FUNWAVE has a parameterization of turbulent dissipation and bottom friction. In its more recent implementation, FUNWAVE (whether Cartesian or spherical) has been parallelized using the MPI language (Pophet, 2008). The code was thus shown to be very efficient and highly scalable on small to medium size computer clusters (Pophet et al., 2010). These recent parallel versions of FUNWAVE will be used for modeling tsunamis, in the present cases of interest.

3.1.1 Initial conditions for model

In earlier tsunami modeling studies, FUNWAVE has been combined with a preprocessor that generates various tsunami sources (e.g., co-seismic, landslide,…), the "Tsunami Open and Progressive Initial Conditions System" (TOPICS; see Watts et al., 2003). The FUNWAVE-TOPICS combination, referred to as GEOWAVE, has been validated based on historical case studies of underwater landslide tsunamis (e.g., Watts et al., 2003; Fryer et al., 2004; Day et al., 2005; Greene et al., 2006; Rahiman et al., 2007; Tappin et al., 2008), earthquake generated tsunamis (Day et al., 2005; Grilli et al., 2007; Ioualalen et al., 2006; 2007), and debris flows (Walder et al., 2006; Waythomas et al., 2006). A new version of the tsunami source preprocessor, which both was implemented in a more user-friendly MATLAB (GUI) environment and whose landslide tsunami source parameterization was updated (see later) will be used in the present simulations.

3.1.2 Co-seismic sources

The standard idealized Okada (1985) method will be used to model co-seismic tsunami sources, as detailed in Appendix A.1. This procedure yields an initial ocean surface elevation, based on the earthquake location, moment magnitude, geographic extent (length, width) and depth, and geological parameters (shear modulus, fault plane dip,

strike and rake angles). Note that the slight modification of Okada's method introduced in the original TOPICS will be used here. As summarized in Appendix A.1, this simply allows specifying a somewhat more realistic Gaussian-like distribution of slip within the fault plane.

3.1.3 Submarine mass failures

As planned at the onset of this project, tsunami hazard resulting from potential Submarine Mass Failures (SMFs) along the US east coast, from Florida to Maine, will first be studied using Monte Carlo Simulations (MCS), based on the probabilistic slope stability analyses of Grilli et al. (2009). This will allow defining and parameterizing a series of potential slope failures (slides or slumps), for which SMF tsunami sources will be developed and FUNWAVE simulations performed, following the methodology outlined in Watts et al.'s (2003, 2005). These sources, which are detailed in Appendix A.2, are based on semi-empirical (curve) fits derived from a large number of full 3D SMF tsunami generation simulations (Grilli et al., 2002; Grilli and Watts, 1999, 2005; Watts et al., 2005). SMF tsunami source parameters are based on the slide specific density, landslide length, maximum thickness and width, mean initial depth, and mean initial incline angle, as well as the location and angle (direction) of the landslide.

3.1.4 Subaerial landslide sources

As discussed above for the CVV case study, tsunami generation by subaerial landslides will be modeled using the 3D-Navier-Stokes model THETIS (Abadie et al., 2009, 2010, 2011), which solves for the velocity and pressure of all three phases: water, air, and landslide. Similar to the model coupling of Løvholt et al. (2008) for the CVV case, THETIS will be coupled to FUNWAVE to simulate the 2D-horizontal ocean-scale tsunami propagation and coastal impact. Specifically, in this one-way model coupling approach, THETIS is used to simulate the first few minutes (10 mins. or so) of the subaerial event and initial (near-field) tsunami generation that results. FUNWAVE is then initialized with the calculated sea surface height and depth-averaged horizontal velocity to perform far-field simulations.

3.2 Sources

3.2.1 Submarine mass failures

For the purposes of modeling SMFs tsunamis along the U.S. East coast, as indicated, most sources will be derived from a separate MCS analysis. Additionally, specific SMF sources will be designed based on the best available data (see Table 4) and used to simulate tsunamis generated by two well-known large underwater landslides, off of the US East coast : (i) the Currituck, and the Grand Banks 1929, landslides. Fig. 4 shows a preliminary simulation of the initial stages of tsunami propagation for case (i).

Parameter	Grand Banks (1929)	Currituck landslide
Location	44.691° N 56.006° W	36.5° N 74.5° W
Direction	170°	100°
Slope incline	6°	4°
Bulk density	2,000 kg/m^3	2,000 kg/m^3
Thickness	5 m	250 m
Length	135 km	30 km
Width	260 km	20 km
Water depth	1,687 m	

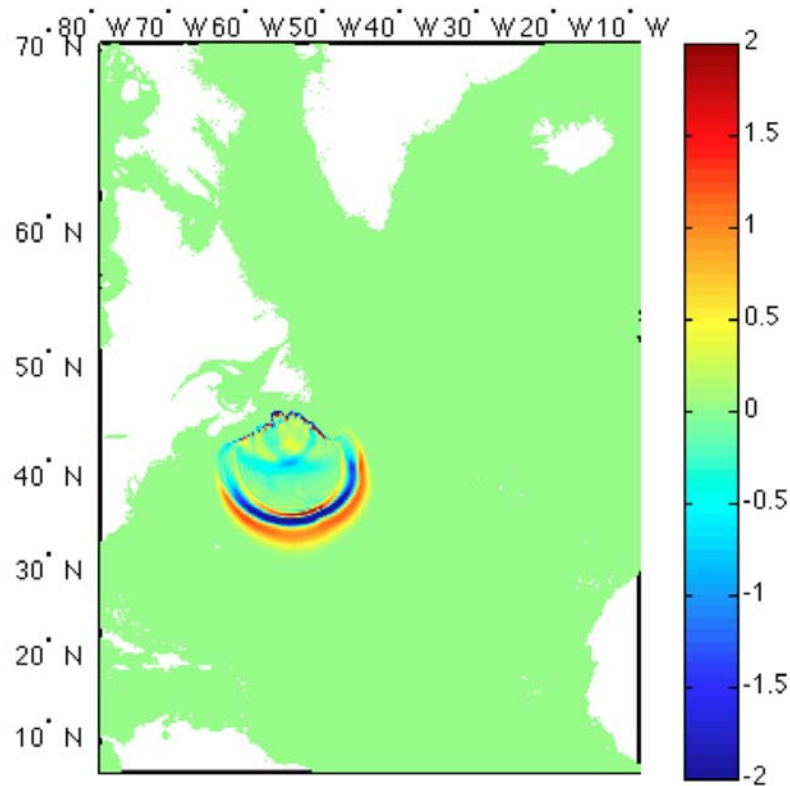Table 4: List of parameters for designing tsunami sources for two past SMFs.

Fig. 11: FUNWAVE simulation of tsunami elevation (m) caused by a SMF similar to the Grand Banks 1929 event. Parameters of the slide are given in Table 4.

3.2.2 Co-seismic tsunamis

Co-seismic tsunami sources with the potential to cause tsunami hazard along the US East Coast have been identified in two areas : (i) the Caribbean subduction zone; and (ii) in the Azores convergence zone.

Regarding area (i), if we focus on earthquakes in the Puerto Rico Trench (PRT) as the most likely sources of tsunami generation, a preliminary list of potential sources would be available from both historical events and predicted earthquake parameters based on plate convergence rates and other known geological information (e.g., Mercado and McCann, 2001; Grilli et. al., 2010a). Table 5 summarizes selected sets of geological parameters for tsunamigenic earthquakes around the PRT. The first 12 sets are identical to sources 48-53, *a* and *b*, of the NOAA Forecast Source Database, and the remaining sets are examples that could be used to test the sensitivity of tsunami generation to various parameters.

Longitude	Latitude	Strike Angle	Dip Angle	Depth (km)
-63.8800	18.8870	95.37	20.00	21.10
-63.8382	19.3072	95.37	20.00	5.00
-64.8153	18.9650	94.34	20.00	22.10
-64.7814	19.3859	94.34	20.00	5.00
-65.6921	18.9848	89.59	20.00	22.10
-65.6953	19.4069	89.59	20.00	5.00
-66.5742	18.9484	84.98	20.00	22.10
-66.6133	19.3688	84.98	20.00	5.00
-67.5412	18.8738	85.87	20.00	22.10
-67.5734	19.2948	85.87	20.00	5.00
-67.4547	18.7853	83.64	20.00	22.10
-68.5042	19.2048	83.64	20.00	5.00
-66.6133	19.3688	94.98	20.00	5.00
-66.6133	19.3688	74.98	20.00	5.00
-66.6133	19.3688	84.98	10.00	5.00

Table 5: Geological parameters for potential co-seismic tsunami sources in the PRT.

Magnitude (M_W)	Moment M_0 (Nm)	Area $A(km^2)$	Length $L(km)$	Width $W(km)$	Slip $\Delta u(m)$
6.5	6.3×10^{18}	224	28	8	.56
7.0	3.5×10^{19}	708	50	14	1.00
7.5	2.0×10^{20}	2,239	89	25	1.78
8.0	1.1×10^{21}	7,079	158	45	3.17
8.5	6.3×10^{21}	22,387	282	79	5.66
9.0	3.5×10^{22}	70,794	501	141	10.0
9.5	2.0×10^{23}	223,872	891	251	17.8

Table 6: Relationship between different parameters for tsunamigenic earthquakes (Ward, 2001). Table 5 does not include events magnitude and area (i.e., length and width), from which an average fault slip can be obtained. In the absence of more detailed information, Ward (2001) defined typical relationships between earthquake parameters (Table 6), which could be useful for designing sources.

Fig. 12 shows a typical simulation with FUNWAVE of the generation and early propagation of an extreme co-seismic tsunami in the PRT, where geological parameters are identical to those modeled by Grilli et al. (2010a) (Table 2), i.e., location: 19.674° N 65.806° W, strike 92°, dip 15°, rake 50°, depth 40 km, length 600 km, width 150 km, except for an average slip 16.7 m (corresponding magnitude $M_w = 9.1$) and shear modulus 4.2×10^{10} Pa (decay radius 200 km, depth of slip 400 m, and water depth 7,000 m).
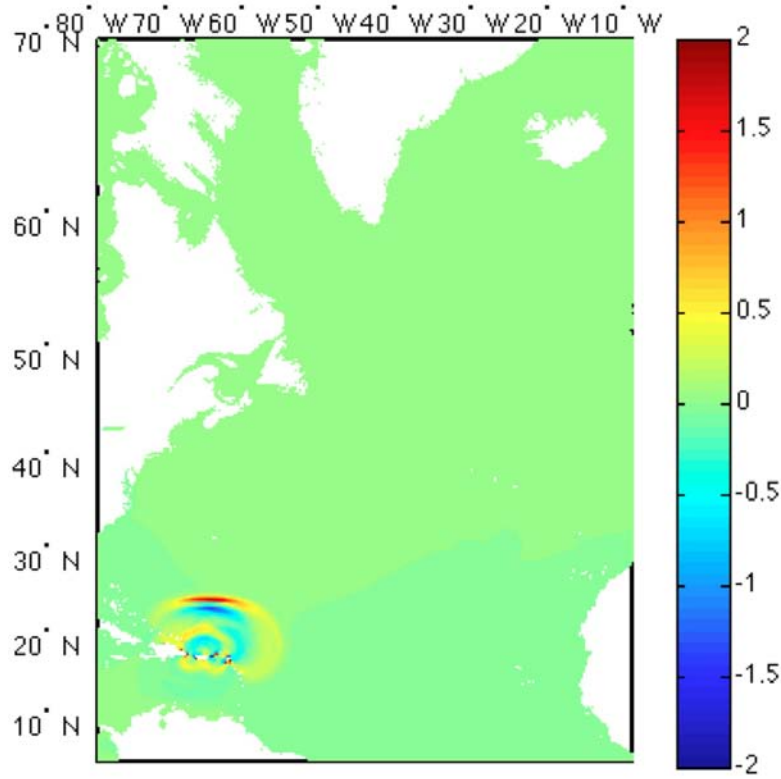

Fig. 12: FUNWAVE simulation of tsunami elevation (m) caused by an earthquake in the PRT, with geological parameters identical to those modeled by Grilli et al. (2010a) (Table 2). Location: 19.674° N 65.806° W, strike 92°, dip 15°, rake 50°, depth 40 km, length 600 km, width 150 km, except for average slip 16.7 m (magnitude $M_w = 9.1$) and shear modulus 4.2×10^{10} Pa (decay radius 200 km, depth of slip 400 m, and water depth 7,000 m).

Regarding area (ii), which is the source of the largest known earthquakes and tsunamis in the north Atlantic basin, a thrust fault with rake of 90° will be used, which results in the highest possible transoceanic tsunami waves (Geist, 1999). Based on ten Brink et al. (2008), a fault strike of 345°, which yields the highest amplitudes in the Caribbean Coasts, will be considered. ten Brink et al. further assumed in their modeling: a dip of 40°, rake of 90º, a source depth of 5 km, fault length of 200 km, width of 80 km, and an average slip 13.1 m (which assuming a shear modulus of 6.5×10^{10} Pa yields a magnitude $M_w = 8.7$). Table 7 specifies selected location of various potential co-seismic sources.

Lat.	35.48	36.21	35.14	37.15	36.04	37.04	36.94	36.01	37.95
Long.	-8.2	-9.82	-10.05	-10.11	-10.75	-10.78	-11.45	-11.46	-12.05

Table 7: Potential earthquake epicenters for the Azores-Gibraltar plate boundary (ten Brink et. al., 2008).

Fig. 13 shows a typical simulation with FUNWAVE of the generation and early propagation of an extreme co-seismic tsunami generated by a source with geological parameters (as discussed above) similar to those of an (estimated) Lisbon 1755 earthquake, i.e., location: 36.015° N 11.467° W, strike 345°, dip 40°, rake 90°, depth 30 km, length 200 km, width 80 km, shear modulus 6.5×10^{10} Pa, average slip 13.1 m (corresponding magnitude $M_w = 8.7$), radius 300 km, depth of slip 40 km, and water depth 4,709 m.
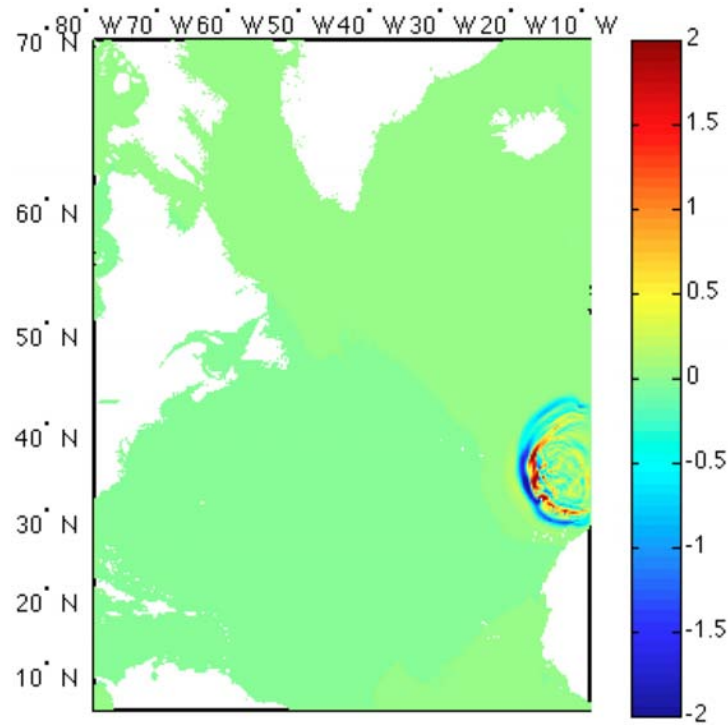

Fig. 13: FUNWAVE simulation of tsunami elevation (m) caused by an earthquake similar to the (estimated) 1755 Lisbon event. Location: 36.015° N 11.467° W, strike 345°, dip 40°, rake 90°, magnitude 8.7, average slip 13.1 m, depth 30 km, length 200 km, width 80 km, shear modulus 6.5×10^{10} Pa (decay radius 300 km, depth of slip 40 km, and water depth 4,709 m).

In the preliminary simulations of both Figs 12 and 13, we see significant tsunami waves propagating towards the US East coast.

3.2.3 Cumbre Vieja Volcano flank collapse

The Cumbria Vieja Volcano (CVV) flank collapse has been identified as an extreme subaerial landslide tsunami source in the Atlantic Ocean basin, with the potential to generate very high and steep near-field waves and significant far-field waves along the US East Coast. As indicated earlier, due to the complexity of both the source mechanism

and the flow in near field waves, the 3D multi-material Navier-Stokes solver THETIS is used to generate the initial conditions, in a fine local grid. As an illustration, Fig. 14 shows snapshots of water and slide interfaces at times up to 10 minutes (volume fractions respectively equal to 0.5 and 0.1) from THETIS' simulation of a subaerial landslide tsunami resulting from a CVV flank collapse scenario, with an initial slide volume of 80 km^3.

        In the case of the CVV, as it would be prohibitive to run FUNWAVE with a structured grid that both resolves the island of La Palma and the entire North Atlantic at the same time, this coupling process is duplicated within FUNWAVE, i.e., a regional Cartesian grid (e.g., 15"x 15") is first used directly around La Palma, to perform tsunami simulations based on THETIS source (e.g., at 10 mins., see Fig. 14c), for the first half hour or so of time, at which point results are saved and re-interpolated onto a coarser spherical grid (e.g., 2'x 2') over the entire North Atlantic Ocean, which is then used to perform FUNWAVE simulations of trans-Atlantic tsunami propagation.
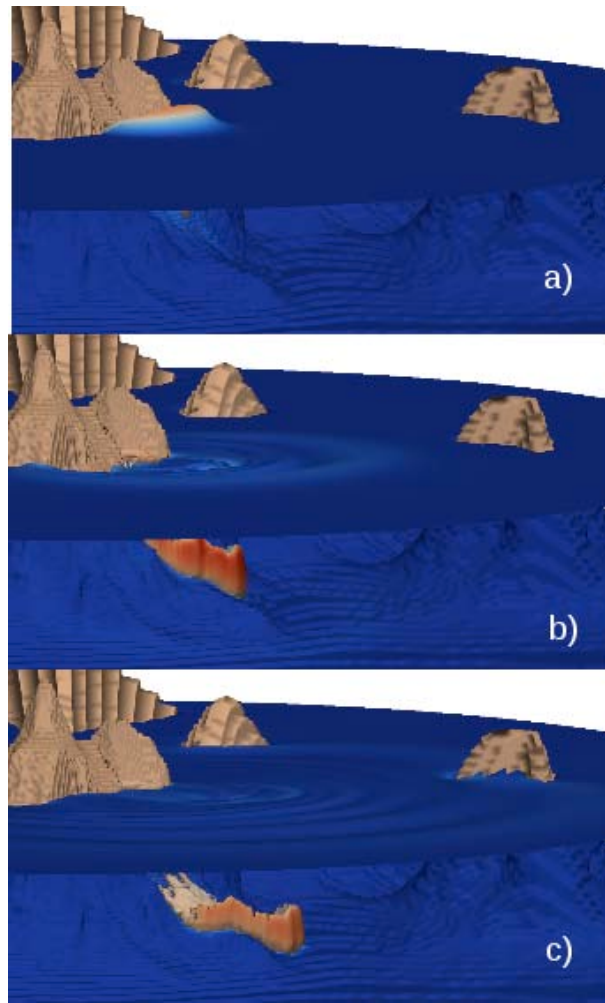

Fig. 14 : THETIS simulation of subaerial landslide tsunami generation by a CVV flank collapse scenario with a slide initial volume of 80 km^3. Snapshots of water and slide interfaces (volume fractions respectively equal to 0.5 and 0.1) at t=: a) 2 min, b) 6 min, c) 10 min into the event.

This is illustrated in Figs. 15 and 16. Fig. 15 shows results in the regional 15" grid, resolving waves directly around La Palma at time t = 25 mins., and Fig. 16 shows propagation at time t =5h33', in the 2' trans-Atlantic grid. Note, in the latter preliminary simulations, some artifacts of the model lower boundary condition (sponge layer) are visible as spurious reflection, lower than 15deg. N latitude. These waves, however, would not affect results along the US East Coast and could be easily eliminated by widening the lower boundary sponge layer.
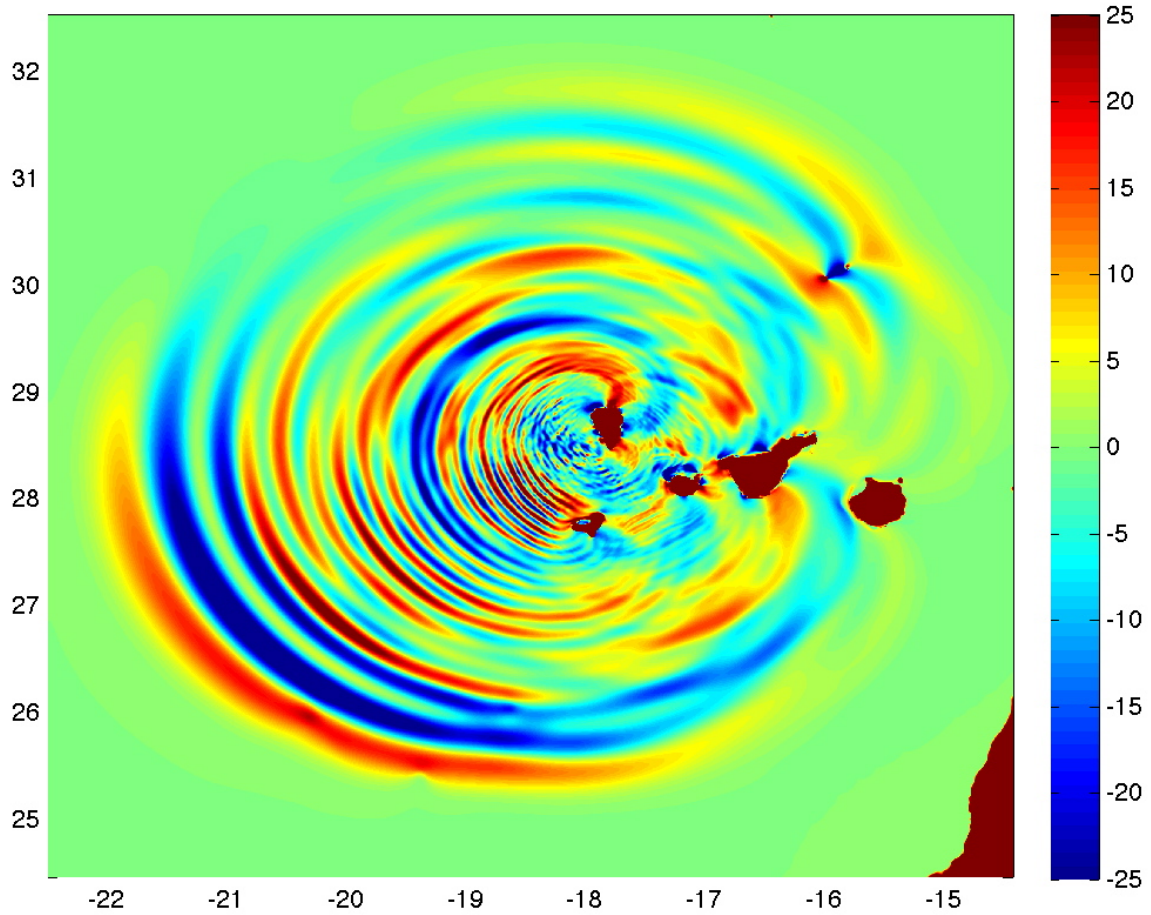

Fig. 15: Case of Fig. 14. (Cartesian) FUNWAVE simulation of tsunami elevation (m) at time t = 25 min, in a regional 15" grid, initialized at t = 512 s using 3D-NS THETIS results (Fig. 14).
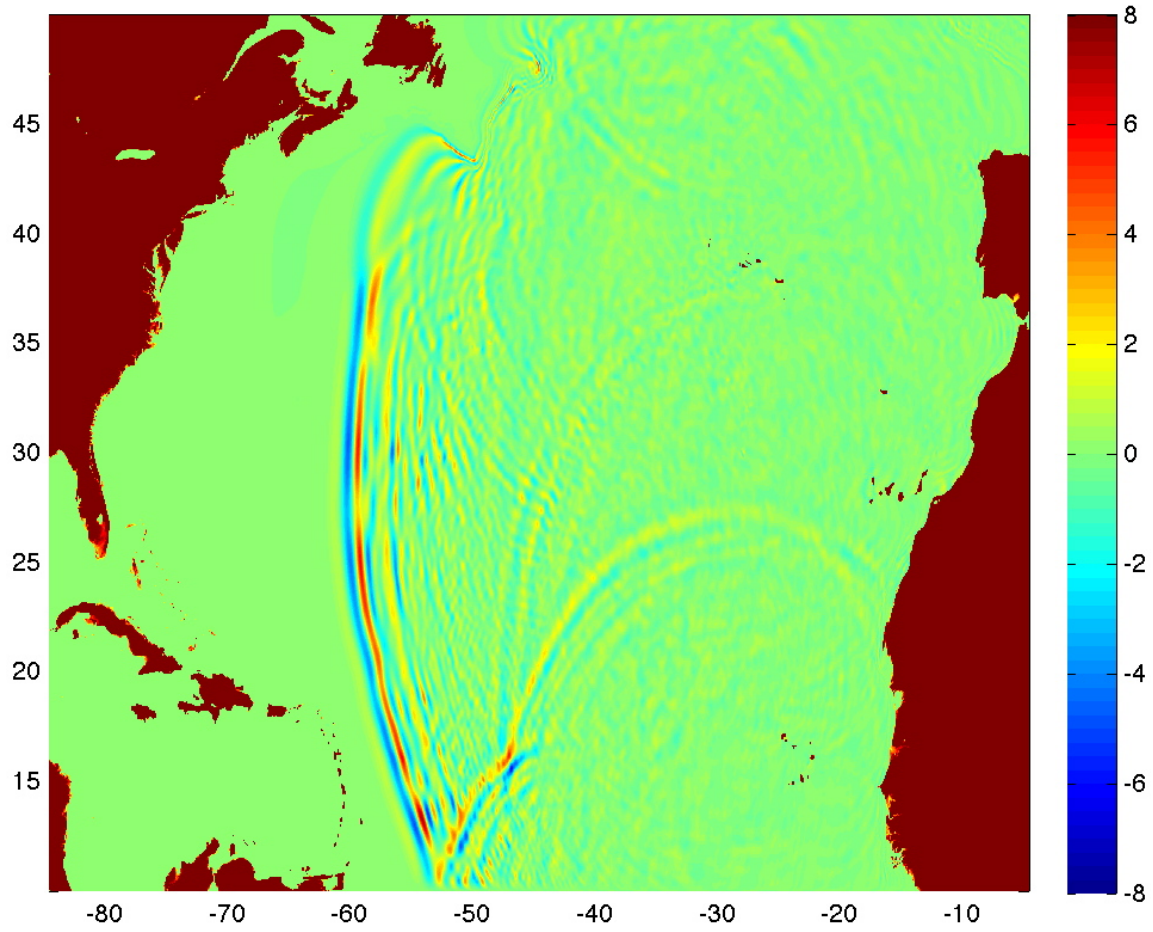
Fig. 16: Case of Figs. 14,15. (Spherical) FUNWAVE simulation of tsunami elevation (m) at time $t =$ 5h33', in a basin scale 2' grid, initialized at $t = 25$' using FUNWAVE regional grid results (Fig. 15).

4. SUMMARY

A literature review demonstrates that tsunami hazard on the U.S. East coast is still not understood well, due to the lack of direct observations and the paucity of historical records. While less frequent than tsunamis in the Pacific ocean, tsunamis would have the potential to cause extensive damage to the densely-populated and low-lying cities of the U.S. East coast.

After considering a large number of the likely sources for tsunamis that would affect the area, including tsunamigenic earthquakes, submarine landslides, and subaerial landslides, a selection of sources was made, for further study of tsunami generation, propagation and inundation with the numerical models FUNWAVE and THETIS. FUNWAVE is a Boussinesq model, which is fully nonlinear in its Cartesian implementation and mildly nonlinear in its spherical implementation, for long wave propagation, that has been successfully used and validated for model tsunami case studies. Further validation was conducted as part of this NTHMP project validation workshop. THETIS is a 3D multi-material Navier-Stokes model, which has been validated for landslide tsunami generation based on standard problems found in the literature (e.g., Russel's wave generator) and for additional cases as part of this NTHMP project validation workshop.

5. APPENDIX A: Implementation of co-seismic and SMF sources

In this NTHMP funded tsunami hazard and inundation work, tsunami propagation and coastal impact simulations are performed using the latest benchmarked version of the fully nonlinear Boussinesq long wave model FUNWAVE (Wei et al., 1995; Chen et al., 2000; Kennedy et al., 2000; Kirby, 2003; Kirby et al., 2009). A preprocessor, referred to as TOPICS for "Tsunami Open and Progressive Initial Conditions System", is used in the model to set-up and initialize a variety of tsunami sources, including co-seismic and SMF (see, e.g., Watts et al, 2003). A summary of FUNWAVE's equations and tsunami implementation can be found in Ioualalen et al. (2007).
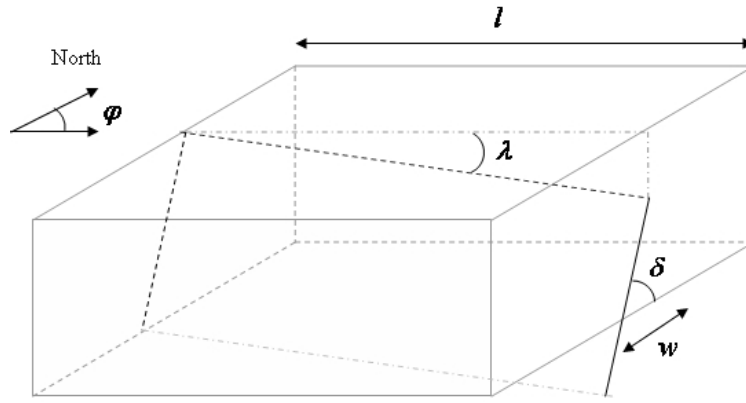

Fig. A1: Sketch of idealized Fault Geometry in Okada's method (1985).

A.1 Co-seismic sources

The modeling and initialization of co-seismic tsunami sources in TOPICS' are based on the standard Okada's (1985) method, with some minor adjustments, which are detailed below. Parameters of the method are three angles orienting the "slip-fault plane" (strike φ, dip δ, rake λ; Fig. A1), the length l and width w of the horizontal rectangular rupture area $A = l\,w$ (centered on the slip plane centroid and with its length oriented in the strike angle direction φ, measured from the geographic North), and material (Lamé) parameters (μ, λ_l). In TOPICS' implementation of Okada's method, maximum fault slip Δ and average slip $\overline{\Delta}$ are obtained from the equation,

$$M_0 = \mu\Delta\int_A f_1 f_2 dx_p dy_p = \mu\overline{\Delta}A \qquad (A1.1)$$

which calculates the total energy M_0 [J] released by an earthquake (related to the earthquake magnitude: $M_w = (\log M_o/1.51) - 6$, by Hanks and Kanamori's relationship), where μ and A are input parameters defined above, and (f_1, f_2) are two empirical functions

(the former being Gaussian-like) describing the assumed shape of the slip distribution within the dislocation plane, given by,

$$f_1 = \exp\left[\frac{-0.6931}{R^2}\left(x_p^2 + y_p^2 + (z_p + D)^2\right)\right] \tag{A1.2}$$

$$f_2 = \exp\left[4.6052\frac{D_0}{z_p}\right] \tag{A1.3}$$

with (x_p, y_p, z_p) the coordinates of points within the dislocation plane in UTM coordinates (x_p and y_p axes are oriented parallel to the sides of the rectangular rupture area and centered on the centroid of the slip plane). We further note that z_p is zero at the earth surface and negative in the interior, R is the radial distance from the centroid of the rupture area for slip to drop to 50% of its maximum value, D_0 is the depth below which slip drops to 1% of its maximum value, and D is the depth of the fault plane centroid. Function f_1 allows to concentrate slip near the center of the slip plane and to control slip decay in an axisymmetric manner from this center, while Function f_2 allows specifying some asymmetry with depth on the plane, in slip distribution, essentially by reducing slip in the shallower region (with respect to the control depth D_0).

For any point (x,y) within area A (x and y are also oriented parallel to the sides of the rectangular rupture area and centered on the centroid of the slip plane), the vertical seafloor elevation is computed as,

$$z(x,y) = -\frac{\Delta}{2\pi}\int_A f_1 f_2\left\{\cos\lambda\left(3\xi\zeta\frac{q}{r_0^5} + f_3\sin\delta\right) + \sin\lambda\left(3\zeta\frac{pq}{r_0^5} - f_4\sin\delta\cos\delta\right)\right\}dx_p dy_p \tag{A1.4}$$

with,

$$\xi = x - x_p \ , \ \eta = y - y_p \ , \ \zeta = -z_p \ , \ r_0 = (\xi^2 + \eta^2 + \zeta^2) \tag{A1.5}$$

$$p = \eta\cos\delta + \zeta\sin\delta \ , \ q = \eta\sin\delta - \zeta\cos\delta$$

$$f_3 = -v\frac{\eta\xi(2r_0 + \zeta)}{r_0^3(r_0 + \zeta)^2} \ , \ f_4 = \frac{v}{r_0(r_0 + \zeta)}\left\{1 - \frac{\xi^2(2r_0 + \zeta)}{r_0^2(r_0 + \zeta)}\right\} \tag{A1.6}$$

In TOPICS, the integrals in Eqs. (1-6) are calculated as sums over a series of ($N \times M$) panels discretizing the slip plane, with (x,y,z) denoting the panel center coordinates.

Once the seafloor elevation is calculated, the horizontal coordinates (x,y) are rotated in the actual strike direction φ of the rupture area. [This is the reason why strike does not explicitly appear in Eqs. (4-6).]

Okada's method assumes a locally flat ocean bottom. However, in tsunami simulations, the actual bottom bathymetry is specified in FUNWAVE, while the tsunami source is expressed at $t = 0$ as an initial free surface elevation with no flow velocity (i.e., cold start).

A.2 SMF sources

The modeling and initialization of Submarine Mass Failure (SMF) tsunami sources in TOPICS' are based on the work of Grilli and Watts (1999, 2001, 2005), Grilli et al. (2002), Watts and Grilli (2003), Watts et al., (2003, 2005), Enet and Grilli (2003, 2007). The latter work deals with the modeling and laboratory experiments of rigid underwater slides (i.e., translational) and slumps (i.e., rotational).
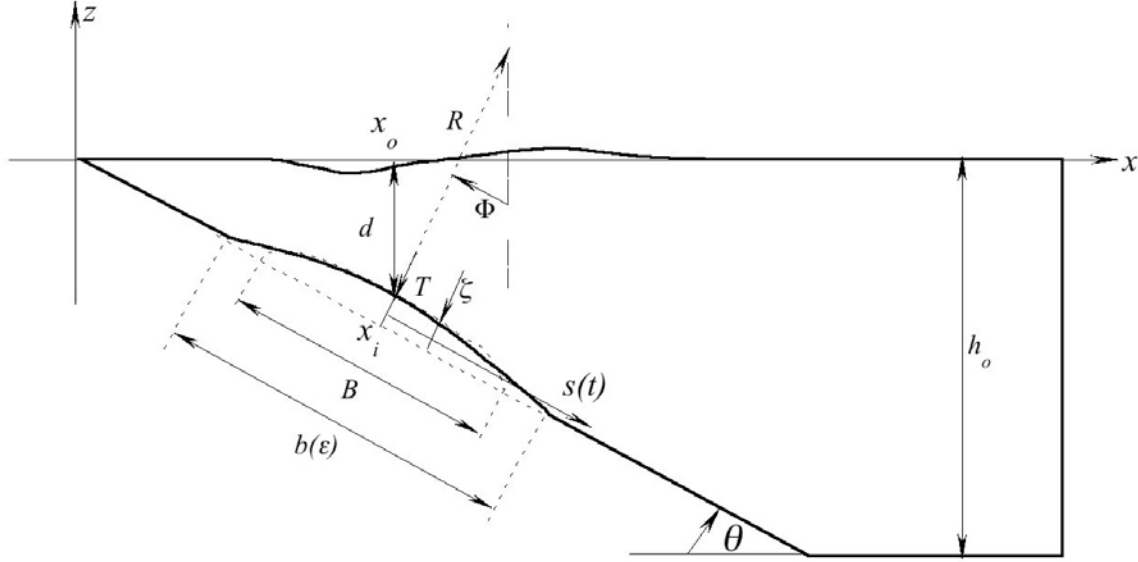

Fig. A2: Parameters definition for 2D cross-section in slide or slump (from Grilli and Watts, 2005)

In this initial computational work, which led to TOPICS, both slides and slump were first considered as wide rigid bodies of 2D semi-elliptical cross-section with major semi-axis $B/2$ and minor semi-axis T (width $w >> B$), sliding on a plane slope of angle θ in a fluid of density ρ_w (Fig. A2; Grilli and Watts, 1999, 2005). The landslide has an average bulk density ρ_b, and its middle location on the slope is initially located at abscissa x_i. Hence,

$$x_i = x_o - T \sin\theta \quad \text{with} \quad x_o = \left(d + \frac{T}{\cos\theta}\right)\frac{1}{\tan\theta} \qquad (A2.1)$$

where x_o is the abscissa on the slope of the location of maximum thickness on the slope. Once the slide motion has been triggered (e.g., by an earthquake), it is assumed that basal friction between slide and slope is negligible and that friction is limited to a global hydrodynamic drag force (with drag coefficient C_d) acting on the slide cross section. Similarly, water inertia effects are represented by a global added mass (with added mass coefficient C_d). For such 2D bodies, the volume and cross-section are simply,

$$V_s = \frac{\pi}{4} wBT \quad \text{with} \quad A_s = wT \qquad (A2.2)$$

A.2.1 2D underwater slides

Rigid translational slide motions are modeled as the displacement *s(t)* of their center of mass (Fig. A2), which is found based on an equilibrium of inertia, added mass, gravity, hydrodynamic drag and buoyancy forces as,

$$s(t) = s_o \ln\left(\cosh\left(\frac{t}{t_o}\right)\right) \quad \text{with} \quad s_o = \frac{u_t^2}{a_o} \quad \text{and} \quad t_o = \frac{u_t}{a_o} \tag{A2.3}$$

with the initial acceleration and terminal velocity,

$$a_o = g\sin\theta\left(\frac{\gamma-1}{\gamma+C_m}\right) \quad \text{and} \quad u_t = \left(gB\sin\theta\frac{\pi(\gamma-1)}{2C_d}\right)^{\frac{1}{2}} \tag{A2.4}$$

respectively, $\gamma = \rho_b/\rho_w$ and *g* denoting the gravitational acceleration.

For such slides, Grilli and Watts (1999, 2005) performed many 2D simulations, using a fully nonlinear potential flow model, and Watts et al. (2005) derived a semi-empirical expression for the minimum surface depression η_o computed at $x = x_o$, referred to as the *characteristic tsunami amplitude*, based on 32 cases of 2D slide simulations, for various combinations of governing parameters: *B, T, d, θ, γ,* using approximate orders of magnitude values for the hydrodynamic coefficients, $C_d = C_m = 1$,

$$\eta_o = s_o(0.0592 - 0.0636\sin\theta + 0.0396\sin^2\theta)\left(\frac{T}{B}\right)\left(\frac{B\sin\theta}{d}\right)^{1.25}(1-e^{-2.2(\gamma-1)}) \tag{A2.5}$$

This equation predicts over 99% of the variance of the computed values of η_o (R^2 = 0.991) and is based on the following ranges of parameter values (in non-dimensional form) in the computations: $\theta \in [5,30]$ deg., $d/B \in [0.06,1.5]$, $T/b \in [0.008,0.2]$, and $\gamma \in [1.46,2.93]$. [Note, Eq. A2.5 has been slightly extended to provide higher accuracy, as compared to Eq. (2) in Watts et al. (2005)]. See Fig. A3a for a comparison of computed values of η_o to predicted values from Eq. A2.5, for the 32 computed slides.

A.2.2 2D underwater slumps

Slumps are modeled as rigid SMFs of maximum angular displacement $\Delta\phi = \phi - \phi_o$ of their center of mass (Fig. A2). Assuming a nearly circular rupture surface of radius *R* and a small angular displacement (with $\sin\phi \approx \phi$), the slump translation *s(t)* along the slope (approximated by the chord of the rupture surface) is found based on an equilibrium of inertia, added mass, gravity, and buoyancy forces as,

$$s(t) = s_o\left(1-\cos\left(\frac{t}{t_o}\right)\right) \quad \text{with} \quad s_o = \frac{\Delta s}{2} \quad \text{and} \quad t_o = \left(\frac{R(\gamma+C_m)}{g(\gamma-1)}\right)^{\frac{1}{2}} \tag{A2.6}$$

Note, hydrodynamic friction has been neglected in these equations because of the lower slump velocities (as compared to slides) and basal Coulomb friction (with coefficient C_n) is implicitly included in the specified angular displacement; thus, assuming a circular rupture surface of radius of curvature R, we find,

$$\Delta s = R(\Delta\phi) = 2RC_n\cos\theta \tag{A2.7}$$

where Δs is the maximum slum linear displacement and other definitions are as before.

For such slumps, Grilli and Watts (2005) performed many 2D simulations, using a fully nonlinear potential flow model, and Watts et al. (2005) derived a semi-empirical expression for the minimum surface depression η_o computed at $x = x_o$, based on 12 cases of 2D slumps simulations, for various combinations of governing parameters: $B, T, d, \theta, \gamma, \Delta s$, using an approximate order of magnitude value for the hydrodynamic coefficient: $C_m = 1$,

$$\eta_o = s_o\left(\frac{T}{B\sin\theta}\right)\left(\frac{B\sin\theta}{d}\right)^{1.25}\left(\frac{B}{R}\right)^{0.60}(\Delta\phi)^{0.39}(\gamma-1)(0.198-0.0483(\gamma-1)) \tag{A2.8}$$

This equation predicts over 99% of the variance of the computed values of η_o ($R^2 = 0.998$) and is based on the following ranges of parameter values in the computations: $\theta \in [10,30]$ deg., $d/B \in [0.34,0.5]$, $T/b \in [0.10,0.15]$, $R/b \in [1,2]$, $\Delta\phi \in [0.1,0.52]$ and $\gamma \in [1.46,2.93]$. As noted by Watts et al. (2005), owing to the similar slide and slump geometry and the identical parameterization found in Eqs. A2.5 and A2.8 for T/B and d/b, one can extend the validity of Eq. A2.8 to $d/B \in [0.06,0.5]$, $T/b \in [0.10,0.2]$ [Note, Eq. A2.8 has been re-derived to provide higher accuracy, as compared to Eq. (4) in Watts et al. (2005)]. See Fig. A3b for a comparison of computed values of η_o to predicted values from Eq. A2.8, for the 12 computed slumps.

A.2.3 3D underwater slides and slumps

In parallel with the 2D slide and slump modeling studies, Grilli et al. (2002) performed a limited number of three-dimensional (3D) of tsunami generated by underwater slides of bulk density ρ_b in water of density ρ_w, on a plane slope of angle θ. These simulations were later extended and experimentally validated by Enet and Grilli (2003, 2005, 2007) (see also Grilli et al., 2010b). The computational model set-up and parameters for these 3D slides is such as shown in Fig. A4 and the experimental set-up is shown in Fig. A5.
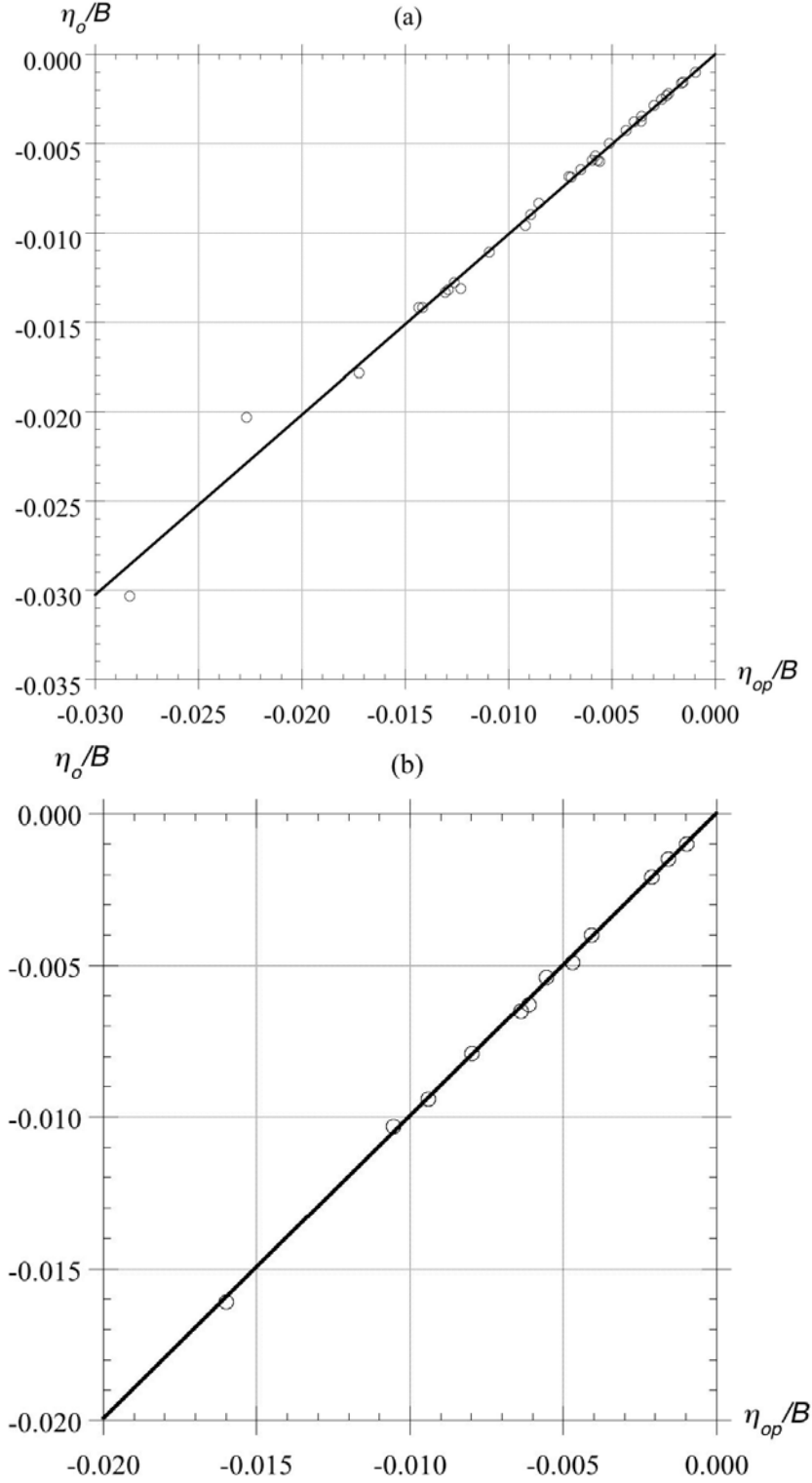
Fig. A3: Comparison of computed η_o versus predicted η_{op} minimum surface depression at $x = x_o$, for 2D underwater: (a) slides (32) using Eq. A2.5; or (b) slumps (12) using Eq. A2.8.

3D Slide/slump tsunami source characteristic amplitude

Although the 3D underwater SMFs that were numerically modeled and tested had a double Gaussian-like geometry, to compare results with earlier 2D work, an equivalent semi-ellipsoidal slide having the same volume and proportions as the original slide is calculated, with length B, thickness T, and width W. The water depth above the initial location, $x = x_o$, of slide maximum thickness is again defined as d.
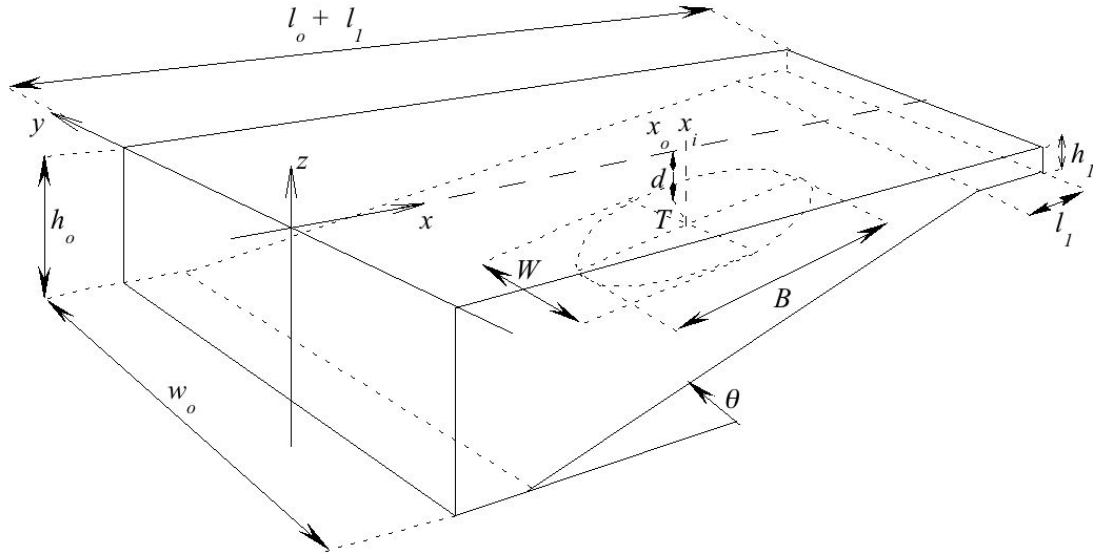

Fig. A4: Parameters definition for 3D slide computations (from Grilli et al., 2002).
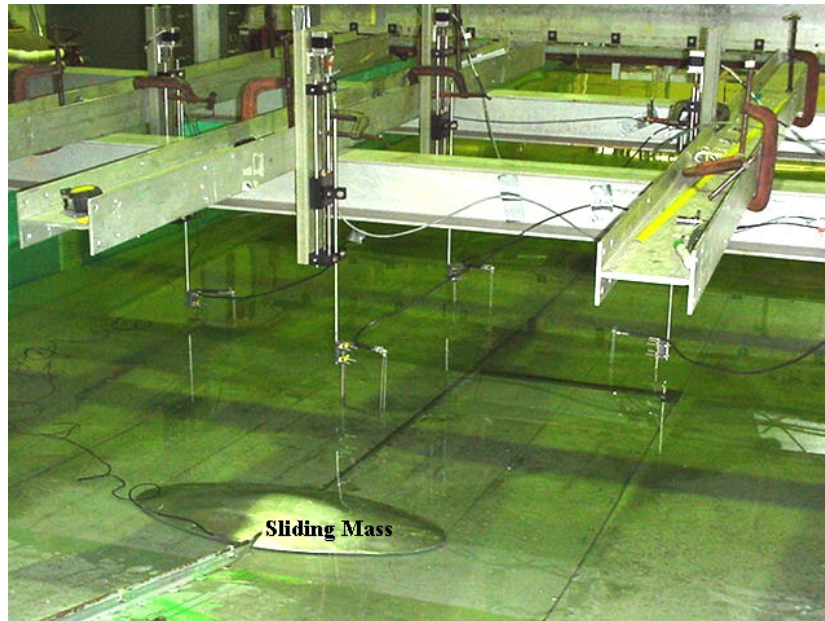

Fig. A5: Experimental set-up for Enet and Grilli's (2003, 2005, 2007) experiments for a rigind 3D slide of Gaussian shape (with elliptical footprint) sliding down a 15 deg. plane slope for a variety of initial submergence d.

The 3D slide volume and main cross-section are thus found for the semi-ellipsoid as,

$$V_s = \frac{\pi}{6} WBT \quad \text{with} \quad A_s = \frac{\pi}{4} WT \tag{A2.9}$$

and slide motion is again modeled with equations A2.3 and A2.4.

Grilli et al. (2002), Enet and Grilli (2005) and Grilli et al. (2010b) simulated surface elevations generated by 3D slides and found that they are all qualitatively similar to those shown in Fig. A6, which corresponds to a rigid slide (of Gaussian shape) moving down a $\theta = 15$ deg. slope, with an initial submergence $d = 0.120$ m ($x_o = 0.764$, from Eq. A2.1). The sub-figures A6 correspond to time: $t = t_o/4$; (b) $t_o/2$; (c) $3t_o/4$; and (d) t_o (vertical scale is exaggerated), with other parameters being identical to those of laboratory experiments by Enet and Grilli (2007). Their laboratory model slide had a specific density $\gamma = 2.435$ and a Gaussian shape with dimensions ($b(\varepsilon) = 0.395$, $w = 0.68$, $T = 0.082$) m (see Figs. A2, A5), but applying Grilli and Enet's transformation equations, we find the dimensions (B, W, T) of an equivalent semi-ellipsoid slide, with same volume and proportion as the Gaussian shape slide (i.e., $b/B = w/W$, Fig. A4). These equations also allow finding the relationship between the kinematics of the 3D Gaussian shape slide of Enet and Grilli (2007) and that of the equivalent semi-ellipsoid, i.e.,

$$a_o = g\sin\theta\left(\frac{\gamma - 1}{\gamma + C_m}\right) \quad , \quad u_t = \left(4gB\sin\theta\frac{(\gamma - 1)}{3C_d'}\right)^{\frac{1}{2}} \text{, with } C_d' = C_d\sqrt{\frac{8(\chi - \varepsilon)^2}{3\pi(1 - \varepsilon)(\chi^2 - \varepsilon)}}$$

$$C = \text{acosh}\left(\frac{1}{\varepsilon}\right) \;\; ; \;\; \chi = \frac{2}{C}\text{atan}\sqrt{\frac{1 - \varepsilon}{1 + \varepsilon}} \;\; ; \;\; B = b\sqrt{\frac{6}{\pi}\frac{\chi^2 - \varepsilon}{1 - \varepsilon}} \;\; \text{and} \;\; W = \frac{B}{b}w \quad \text{(A2.10)}$$

where C_m and C_d are hydrodynamic coefficients found by curve fitting the measured 3D Gaussian slide motion using the slide kinematics equations (Eqs. 9 and 10 in Enet and Grilli, 2007). Note that if one uses the earlier formulation of the slide kinematics A2.4, the drag coefficient is: $C_d'' = (3\pi/8) \, C_d'$. Also note that, in the absence of such detailed experimental measurements, these coefficients had been approximated to $C_m = C_d = 1$ in the earlier work of Grilli and Watts (2005) and Watts et al. (2005) for 2D SMFs.

Thus, for the equivalent 3D semi-ellipsoid slide kinematics, described by Eqs. A2.10, we find that the added mass coefficient does not change as compared to the original slide, but the viscous drag coefficient C_d' depends on slide shape, which is parameterized as elevation ζ (Fig. A2), in axes (ξ, ν) by coefficient ε as,

$$\zeta(\xi, \nu) = \frac{T}{1 - \varepsilon}\left\{\text{sech}\left(\frac{2C\xi}{b}\right)\text{sech}\left(\frac{2C\nu}{w}\right) - \varepsilon\right\} \tag{A2.11}$$

For their experimental slide, Enet and Grilli (2007) reported $\varepsilon = 0.717$, which yields using Eq. A2.10: $C = 0.862$, $\chi = 0.895$, $C'_d = 1.062\ C_d$ (and $C''_d = 1.251 C_d$), and dimensions: $B = 0.298$ m, $T = 0.082$ m, $W = 0.513$ m, for the semi-ellipsoid. Now, for the case of Fig. A6, with $d = 0.12$ m, we find $C_m = 0.685$ and $C_d = 0.332$ in Enet and Grilli's (2007) Table 1, to match the experimentally measured slide motion. Hence, applying Eqs. A2.3 and A2.10, we find $t_o = 1.74$ s and $s_o = 3.52$ m.

To compare the experimentally measured initial surface depressions, referred to as the tsunami source characteristic amplitude, to those predicted in computations, one can of course perform fully nonlinear 3D computations, such as shown in Fig. A5, for each specific case. Doing so, Enet and Grilli (2005, 2007) and Grilli et al. (2010b) found a very good agreement between experimental and computed surface elevations at a number of gages, as a function of time. However, because of the high computational cost of such 3D simulations, as was done for 2D SMFs, it is desirable to derive semi-empirical equations that can be used to quickly define landslide tsunami source elevation in practical situations, as a function of a few governing parameters. Watts et al. (2005) already attempted to do so by observing, based on the limited number of 3D computations of Grilli et al. (2002), that the initial surface depression in 3D, η_o^{3D}, decreased as a function of the ratio of the characteristic tsunami wavelength λ_o (Grilli and Watts, 1999, 2005) to the SMF width, approximately as,

$$\eta_o^{3D} \cong \eta_o \frac{1}{1+\dfrac{\lambda_o}{W}} \quad \text{with} \quad \lambda_o = t_o\sqrt{gd} \tag{A2.12}$$

where η_o is the 2D characteristic amplitude given by equations A2.5 and A2.8, for slides or slumps. Enet and Grilli (2007) applied this equation to the original semi-empirical equations derived by Watts et al. (2005) for 2D slides, and reported a good agreement with their measurements of η_o^{3D}.

Here, as a validation of the proposed equations for TOPICS, we have combined the improved formulation of the 2D characteristic amplitude given by Eq. A2.5 and re-derived a best fit for Eq. A2.12 for the lateral 3D spreading effect, by applying the equations to all the experimental cases of Enet and Grilli (Table 1), for non-breaking waves, which correspond to submergences: $d = 0.061 - 0.189$ m. In each case, we used the reported values of C_m, which range from 0.582 to 0.767 (mean 0.637, st.d. 0.067), and C_d, which range from 0.302 to 0.509 (mean 0.386, st.d. 0.076). This yields,

$$\eta_o^{3D} = \eta_o \frac{0.935}{\left(1+\dfrac{\lambda_o}{W}\right)^{0.872}} \quad \text{or} \quad \eta_o^{3D} = \eta_o 0.535 e^{-0.211\frac{\lambda_o}{W}} \quad \text{with} \quad \lambda_o = t_o\sqrt{gd} \tag{A2.13}$$

with the second formulation providing a slightly better fit, when combined with Eq. A2.5 than the first one, and explaining over 96% of the experimental variance ($R^2 = 0.961$).
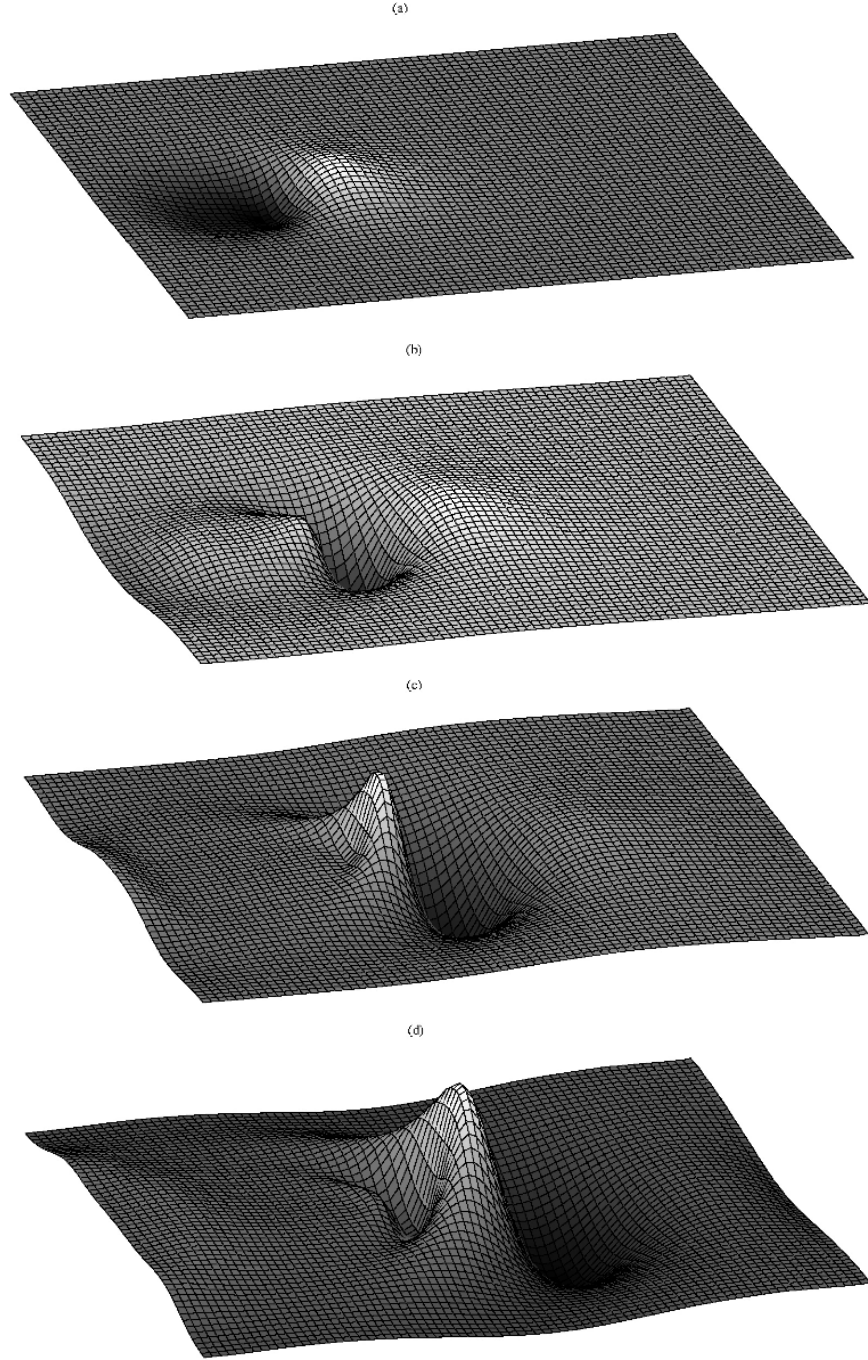
Fig. A6: Example of free surface elevation computed for a 3D SMF, sliding over a θ = 15 deg. slope, at time $t = t_o/4$; (b) $t_o/2$; (c) $3t_o/4$; and (d) t_o (vertical scale is exaggerated). The slide equivalent semi-ellipsoid has dimensions : B = 0.298 m, T = 0.082 m, W = 0.515 m, with γ = 2.435 and an initial slide submergence d = 0.120 m (x_o = 0.764, from Eq. A2.1), for which t_o = 1.74 s based on Eqs. A2.3 and A2.4, using C_m = 0.685 and C_d = 0.416 to match experimentally measured slide motion (results based on Enet and Grilli, 2005, 2007; Grilli et al., 2010b).

By contrast, using Watts et al. equations as summarized in Grilli and Enet (2007), which include Eq. A2.12, one can explain over 95% of the experimental variance ($R^2 = 0.955$). Fig. A6 shows the comparison of measured and predicted *3D characteristic amplitudes* (i.e., surface depression at $x = x_o$), based on the latter formulation and on the new one, combining Eq. A2.12 with the second Eq. A2.13. The graphical agreement is quite good.
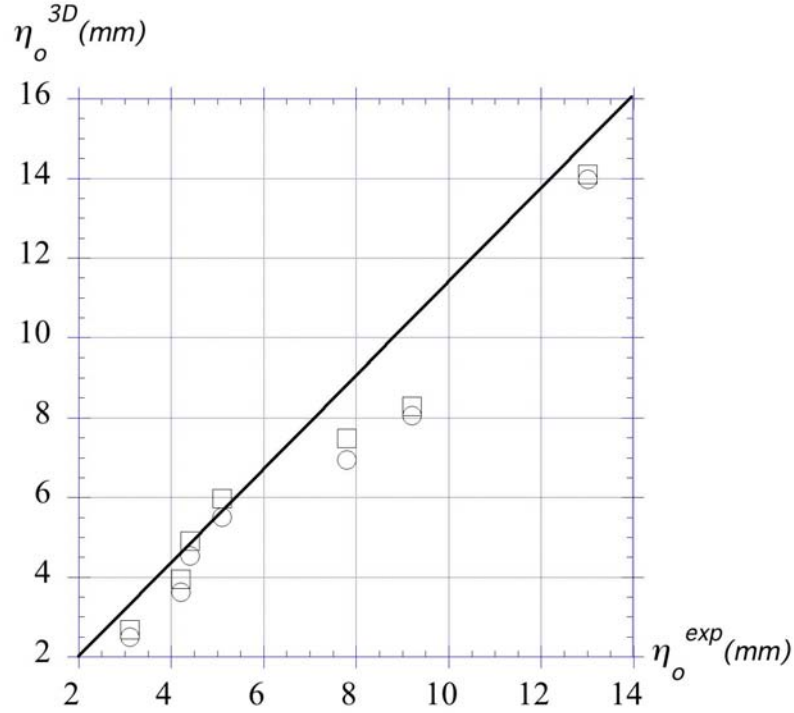

Fig. A7: Experiments of Fig. A5. Prediction of experimentally measured characteristic tsunami depressions η_o^{exp} using : ($\square$) the initial parameterization of Watts et al. (2005) ($R^2 = 0.955$); (o) the newly proposed parameterization using Eqs. A2.5 and 2nd Eq. A2.13 ($R^2 = 0.961$).

3D Slide/slump tsunami source elevation

In 3D, as can be seen in Fig. A6, the free surface shows an initial depression above the slide initial location, with a smaller wave of elevation ahead of it (a); then the 3D wave propagation gradually spreads out these features both forward and laterally, as time increases (b-d); this lateral spreading has a shape similar to a Gaussian-like sech$^2(\kappa y)$ function. A second, crescent shape, elevation wave then gradually grows behind the initial depression and propagates both offshore and onshore (the latter causing runup). In the median vertical plane $y = 0$, the surface elevation appears qualitatively similar for small time $t < t_o$ to that computed for 2D slides (e.g., Grilli and Watts's (2005) Figs. 11 and 12). As was found by Grilli and Watts (2005) in 2D, maximum tsunami generation, defined by the deepest surface depression above the slide instantaneous location, η_{min}, is reached for $t \approx t_o$ (e.g., Fig. A5d), at which time Eq. A2.3 yields a slide displacement: $s_{min} = 0.4338\ s_o$ ($s_{min} = 1.76$ m for the case of Fig. A6, or $x_{min} = 2.24$ m; Eq. A2.1). Additionally, the same work showed that the 2D characteristic tsunami amplitude η_o is

reached for all submergence depths d, they analyzed, at $t \approx 0.5 t_o$ (e.g., Fig. A5b). Finally, in the 2D slides studied by Grilli and Watts (2005) they found across all initial submergences,

$$\eta_{min} \approx (2\text{-}2.5)\ \eta_o \tag{A2.14}$$

Although a similar thorough computational study of 3D slides was not performed by Grilli et al. (2002) and Enet and Grilli (2003, 2005), due to the high computational costs at the time, similar observations were made for 3D slides, at least qualitatively. Thus, in their laboratory experiments for 3D rigid slides, Enet and Grilli (2003, 2005) found that the maximum depression η_o above at $x = x_o$ occurred in the various tested submergences, for $t \approx 0.25\text{-}0.35 t_o$ (i.e., slightly earlier than for 2D slides; their Fig. 14) and with a significantly reduced value, as compared to 2D slides, as a result of 3D wave energy radiation from the initial slide location, as already quantified by Eqs. A2.12 and A2.13.

In view of these salient features of the initial free surface elevation generated by 3D SMFs, and to avoid performing full computations of such 3D tsunami sources, each time this is required to simulate a SMF tsunami in practical situations, Watts and Grilli (2005) proposed a parameterization of the initial tsunami elevation at the time of maximum surface depression $t = t_o$, $\eta(x,y)$ and horizontal (depth-averaged) velocity $\mathbf{u}(x,y)$, to be used as an initial condition in 2D horizontal long wave tsunami propagation models such as FUNWAVE. This parameterization was built around the work of Grilli and Watts (2005), Grilli et al. (2002), and Enet and Grilli (2003, 2005), and uses 2D characteristic amplitude Eqs. A2.5 and A2.8, for slides and slumps, Eqs. A2.12 for the lateral 3D spreading, and other considerations discussed below.

Specifically, in the original TOPICS implementation of Watts et al.'s (2005) parameterization for slides or slumps the surface elevation of the tsunami source was modeled as the sum of two Gaussian functions of x (g_1 and g_2) multiplied by a sech^2 function of y. However, in view of the various new parameterizations proposed, coefficients α_1 and α_2 were added, in order for $\eta_{2D}(x,y)$ to be nearly η_{min} at $x = x_{min}$ and η_{max} at $x = x_{max}$, for $y = 0$, as,

$$\eta_{3D}(x,y,t_o) = \eta_{min} f(W) \operatorname{sech}^2\left(\kappa f(W)\frac{y}{W}\right)\left\{\alpha_1 g_1(x) - \alpha_2 \kappa' g_2(x)\right\}$$

$$g_1(x) = e^{-\left(\frac{x-x_{min}}{\kappa' \lambda_o}\right)^2} \quad ; \quad g_2(x) = e^{-\left(\frac{x-x_{min}-\Delta x}{\lambda_o}\right)^2} \tag{A2.15}$$

$$\alpha_1 = \frac{1+\kappa' g_2(x_{min})}{1-g_1(x_{max})g_2(x_{min})} \quad ; \quad ; \alpha_2 = \frac{1+(1/\kappa')g_1(x_{max})}{1-g_1(x_{max})g_2(x_{min})}$$

with, in the earlier TOPICS parameterization,

$$x_{min} = \Delta x_o - x_o \quad ; \quad \Delta x_o = c_o(x_o + c_1 s_o \cos\theta) \quad ; \quad x_{max} = x_{min} + \Delta x$$

$$\Delta x = c_2 \lambda_o \quad ; \quad \eta_{\min} = -f_1 \eta_o \quad ; \quad \eta_{\max} = f_2 \eta_o \quad ; \quad \kappa' = f_2 / f_1$$

$$f(W) = 1 - \exp\left\{ -c_3 \frac{W}{\lambda_o}\left(1 + c_4 \frac{W}{\lambda_o}\right)\right\} \quad ; \quad \kappa = 3 \tag{A2.16}$$

with $c_3 = 2.091$ and $c_4 = 1.090$ and η_o denoting the 2D characteristic amplitude.

Additionally, for slides, we have,

$$c_o = 0.95 \quad ; \quad c_1 = \log(\cosh(1)) = 0.4338 \quad ; \quad c_2 = 0.5$$

$$f_1 = 2.52 \quad ; \quad f_2 = 0.512\left(1 + 0.25\frac{d}{d_{ref}}\right) \quad ; \quad d_{ref} = B\sin\theta \tag{A2.17}$$

and for slumps,

$$c_o = 0.565 \quad ; \quad c_1 = 1 - \cos(1) = 0.4597 \quad ; \quad c_2 = 0.8 \quad ; \quad S_g = \frac{s_o \sin\theta}{d} = \frac{s_o}{B}\frac{d_{ref}}{d}$$

$$f_1 = 3.479\left(\frac{1 - 1.102 S_g + 1.865 S_g^2}{1 + 3.168 S_g}\right) \quad ; \quad f_2 = 2.057\left(\frac{1 - 0.599 S_g + 1.096 S_g^2}{1 + 2.932 S_g}\right) \tag{A2.18}$$

where S_g denotes the so-called submergence number.

The lateral spreading function $f(W)$ in Eqs. A2.15 and A2.16, although of the same nature, is different from those proposed earlier in Eq. A2.13, on the basis of the experimental validation. This function as well as the sech² function in Eq. A2.15, were parameterized initially in TOPICS, based on Grilli et al.'s (2002) 3D numerical simulations (such as shown in Fig. A6).

In view of the experimental validation presented above, we now use in Eq. A2.15, the new parameterization of the lateral spreading function, corresponding to the second Eq. A2.13, as,

$$f(W) = 0.535\exp\left\{ -0.211\frac{\lambda_o}{W}\right\} \quad \text{with} \quad \kappa = 6 \tag{A2.19}$$

Using Eq. A2.19 to calculate the reduction of 2D characteristic elevations in Eq. A2.15, instead of the earlier parameterization of lateral spreading, we also find that, in order for most of the lateral damping of the 3D surface elevation to occur over four times the width of the slide (i.e., $4W$), in the sech² function of y, as was specified in earlier parameterizations based on Grilli et al.'s 3D computations, one now needs to use a new value of $\kappa = 6$, as indicated in Eq. A2.19.
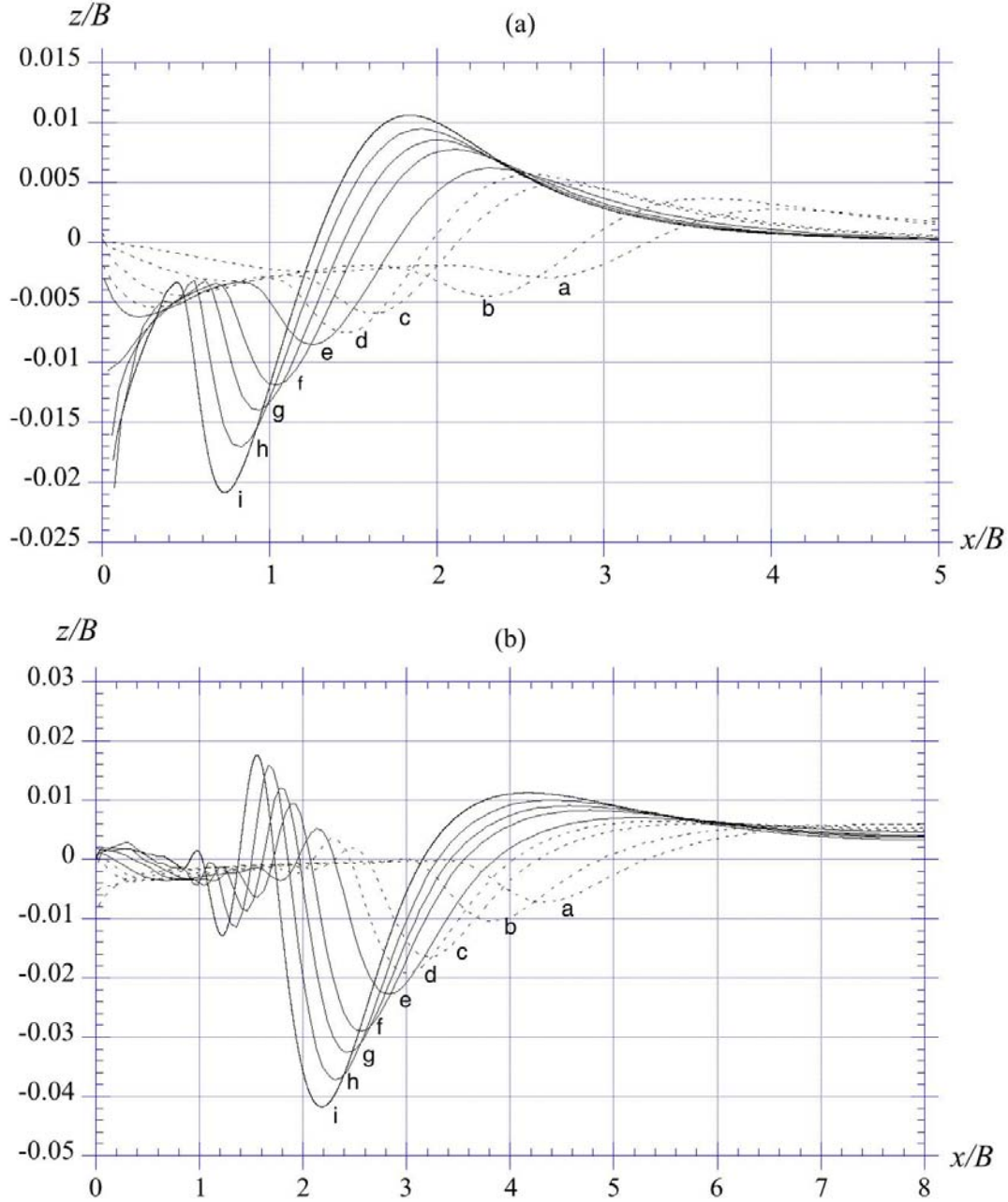
Fig. A8: 2D computations of semi-elliptical underwater slide by Grilli and Watts (2005) (with $\theta = 15$ deg., $B = 1$ m, $T = 0.052$ m, $\gamma = 1.85$, $C_m = C_d = 1$), for initial depth $d =$ a: 0.625; b: 0.5; c: 0.35; d: 0.3; e: 0.259; f: 0.2; g: 0.175; h: 0.15 m, at time: (a) when the maximum depression η_o is reached at $x = x_o$; (b) $t = t_o$.

The rest of Eq. A2.15, which is function of x, was initially parameterized based on 2D numerical simulations (e.g., Fig. 11 in Grilli and Watts, 2005). A more careful re-analysis of the latter computations is done in the following, for a $\theta = 15$ deg. slope, and a 2D semi-elliptical slide with $B = 1$ m, $T = 0.052$ m, and $\gamma = 1.85$. Using $C_m = C_d = 1$, Eqs. A2.3 and A2.4 yield $s_o = 4.477$ m and $t_o = 2.432$ s. Initial submergence is varied

within $d = 0.15$ to 0.625 m (9 depth values); for each of those, Eq. A2.1 yields x_o. Grilli and Watts gave computed free surface profiles as a function of time, which are partly shown in Figs A8a,b, at: (a) the (different) times when the maximum surface depression η_o is reached at $x = x_o$, and (b) at time $t = t_o$, when the absolute free surface minimum η_{min} is reached. New curve fits were calculated on the basis of these results, as (Fig. A9),

$$\eta_{\min} = -f_1\eta_o \quad ; \quad f_1 = 1.10\left\{1 + 2.21\frac{d}{d_{ref}}\left(1 - 0.314\frac{d}{d_{ref}}\right)\right\} \tag{A2.20}$$

$$\eta_{\max} = f_2\eta_o \quad ; \quad f_2 = 0.347\left\{1 + 1.06\frac{d}{d_{ref}}\left(1 + 0.409\frac{d}{d_{ref}}\right)\right\} \tag{A2.21}$$

with $R^2 = 0.943$ and 0.999, respectively.

Over the 9 depth values, the average value of f_1 is 2.60, which is quite close to the 2.52 value used earlier in Eq. A2.17. Based on these results, we also derive the following curve fits (Fig. A10),

$$x_{\min} = \Delta x_o - x_o \quad ; \quad \Delta x_o = c_o(x_o + c_1 s_o \cos\theta) \quad ; \quad c_o = 2.143 \quad ; \quad c_1 = 0.124 \tag{A2.22}$$

$$x_{\max} = x_{\min} + \Delta x \quad ; \quad \frac{\Delta x}{B} = c_{21}\left(1 - c_{22}\frac{\lambda_o}{B}(1 - c_{23}\frac{\lambda_o}{B})\right) \quad ;$$

$$c_{21} = 2.96 \quad ; \quad c_{22} = 0.270 \quad ; \quad c_{23} = 0.211 \tag{A2.23}$$

with $R^2 = 0.998$ and 0.996, respectively. These are quite different from the earlier parameterization for slides used in Eqs. A2.16, A2.17. Fig. A9 shows the relationship between x_{min}, x_{max}, and x_o, which here, for constant slide thickness T and slope angle θ is linearly related to d or d/d_{ref} (Eq. A2.1). Moreover, from Eq. A2.13, we see that, in the present case, λ_o is simply proportional to $d^{1/2}$, which further explains the good linear fit of x_{max} with x_o.

We see in Fig. A8b that the free surface at $t = t_o$ can indeed essentially be approximated by the sum of two Gaussian functions, respectively centered on the location of minimum depression $x = x_{min}$ (negatively) and on that of the first elevation wave downstream of it, defined as $x = x_{max} = x_{min} + \Delta x$ (positively); this confirms the parameterization introduced in Eq. A2.15. Also note in Fig. A8b, the second elevation wave, which follows (upstream) the depression wave at x_{min} (as also seen in Fig. A6d), and is neglected in the parameterization A2.15. One of the reasons for this (besides reducing the complexity of the parameterized source geometry) is that, in numerical or laboratory experiments discussed so far, the entire seafloor was modeled as a surface piercing plane of constant slope, which is likely to significantly enhance this second "rebound" surface elevation wave. In natural shelves, by contrast, for SMFs occurring on the continental shelf slope, this rapid reflection and enhancement do not occur on the
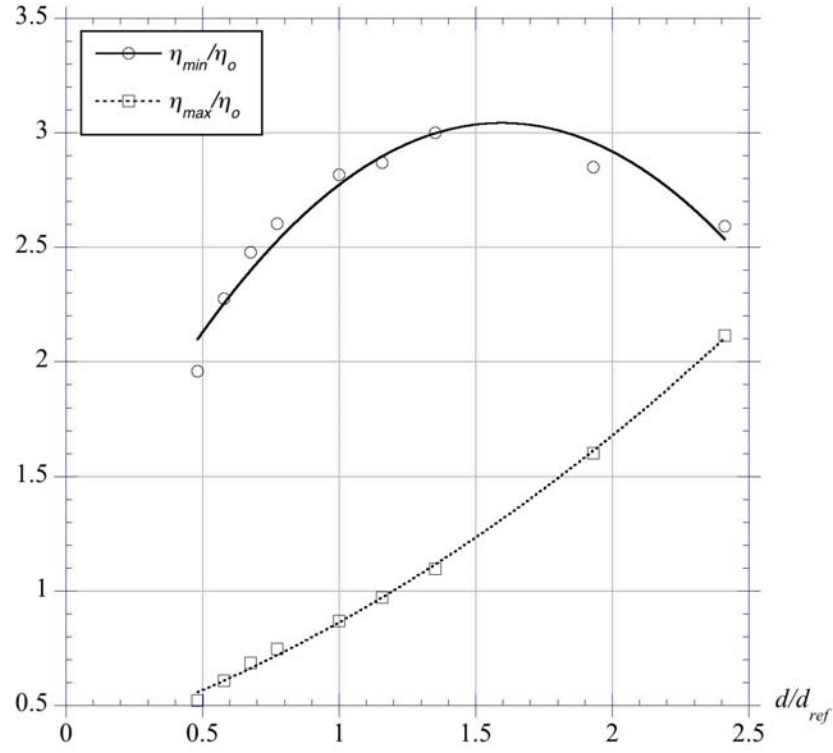
48

Fig. A9: Data and curve fit based on Grilli and Watts' (2005) computations of Fig. A8, for minimum and maximum 2D surface elevations.
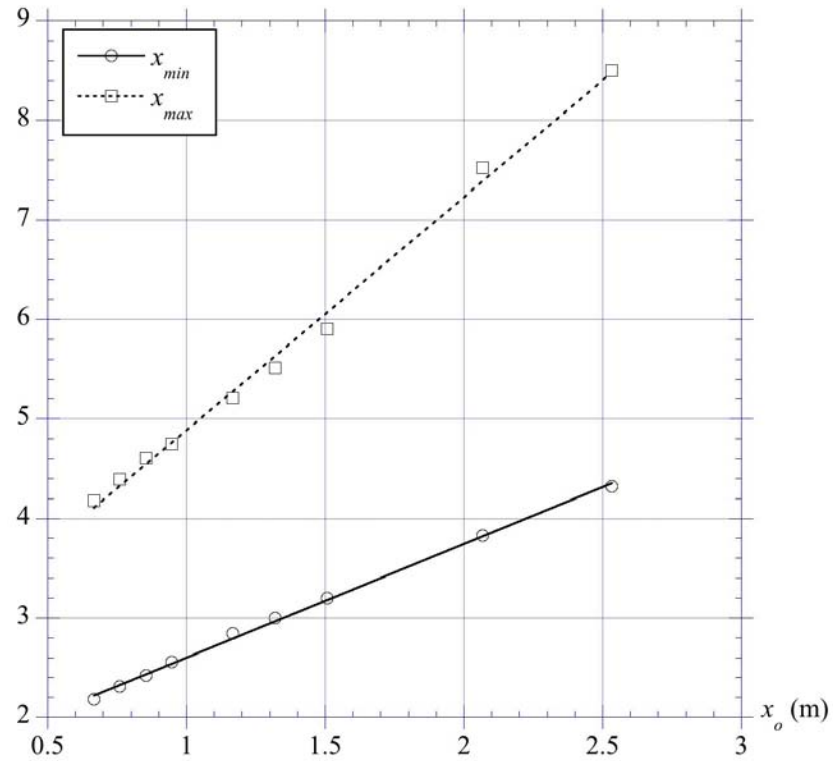

Fig. A10: Data and curve fit based on Grilli and Watts' (2005) computations of Fig. A8, for *x* location of minimum and maximum 2D surface elevations.
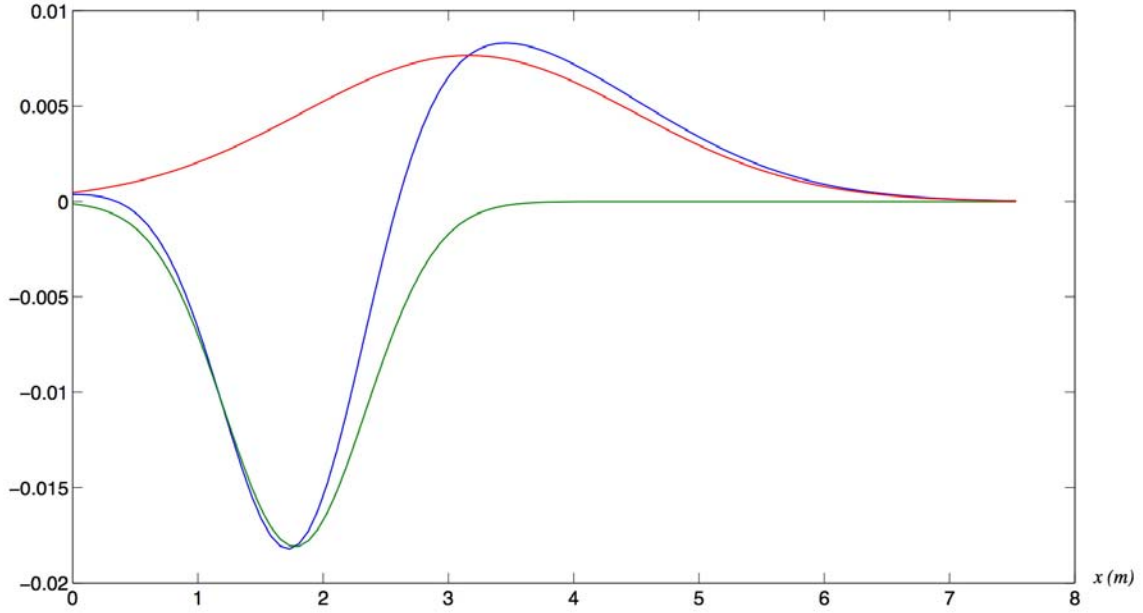
Fig. A11: Free surface elevation $\eta(x,0)$ for $y = 0$, at t_o, (blue line) in empirical tsunami source elevation Eq. A2.15, with parameterization of Eqs. A2.5 and A2.19-A2.23, for the case of Fig. A6 ($\theta = 15$ deg., $B = 0.298$ m, $T = 0.082$ m, $W = 0.515$ m, $\gamma = 2.435$, $d = 0.120$ m), for which $x_o = 0.764$ m, $t_o = 1.74$ s and $s_o = 3.52$ m, using $C_m = 0.685$ and $C_d = 0.416$. The red and green lines show the two Gaussian functions of x in Eq. A2.15.

onshore side, due to the continental shelf over which the second "rebound" wave can spread out.

Using Eq. A2.15 with the parameterization in Eqs. A2.19-A2.23, we now calculate the 3D free surface elevation (i.e., SMF tsunami source) for the case computed in Fig. A6, which corresponds to one of Grilli and Enet's (2007) experiment for a $\theta = 15$ deg. plane slope, and a 3D Gaussian-shape slide with dimensions of the equivalent semi-ellipsoid: $B = 0.298$ m, $T = 0.082$ m, $W = 0.515$ m (Eqs. A2.10), density $\gamma = 2.435$ and an initial slide submergence $d = 0.120$ m (for which $x_o = 0.764$ m, $t_o = 1.74$ s and $s_o = 3.52$ m), using $C_m = 0.685$ and $C_d = 0.416$. For this case, Eqs. A2.5 and A2.19-A2.23 yield: $\eta_o = 0.0242$ m, $\eta_o^{3D} = 0.0060$ m ($\eta_{o,exp}^{3D} = 0.0051$ m), $f(W) = 0.247$, $\eta_{min} = -0.0181$ m ($f_1 = 3.03$), $\eta_{max} = 0.0077$ m ($f_2 = 1.28$), $\kappa' = 0.422$, $x_{min} = 1.777$ m, $x_{max} = 3.160$ m, $\Delta x = 1.383$ m, $\lambda_o = 1.883$ m, and $\Delta x / \lambda_o = 0.734$. For this case, Fig. A11 shows a cross section in free surface elevation: $\eta(x,0)$ for $y = 0$ (blue line), with the two Gaussians of Eq. A2.15 shown (in green and red). We see that the surface elevation at $y = 0$ takes the expected η_{min}, x_{min}, η_{max}, and x_{max} values.

Fig. A12 then shows the full 3D source elevation (i.e., $\eta(x,y)$ at t_o), predicted for this case by Eq. A2.15, which is to be compared with computations of Fig. A6. While the agreement with Fig. A6b (at $t = t_o/2$) appears qualitatively good, due to the appearance of the second (rebound) elevation wave in computations for later time (see above

50

discussion), which is not included in the semi-empirical free surface elevation, the qualitative agreement is less good for Fig. A6d, which is at $t = t_o$, at the time of maximum tsunami generation. However, despite these differences in shape, the empirical solution has a good agreement (not shown here), on the minimum surface depression and maximum elevation, as well as their location, with respect to the starting location of the slide, and good agreement on wavelength (in x direction) and lateral spreading.

Fig. A12: Free surface elevation $\eta(x,y)$ at t_o, i.e., SMF tsunami source, from empirical tsunami source elevation Eq. A2.15, with parameterization of Eqs. A2.5 and A2.19-A2.23, for the case of Fig. A6, A11.
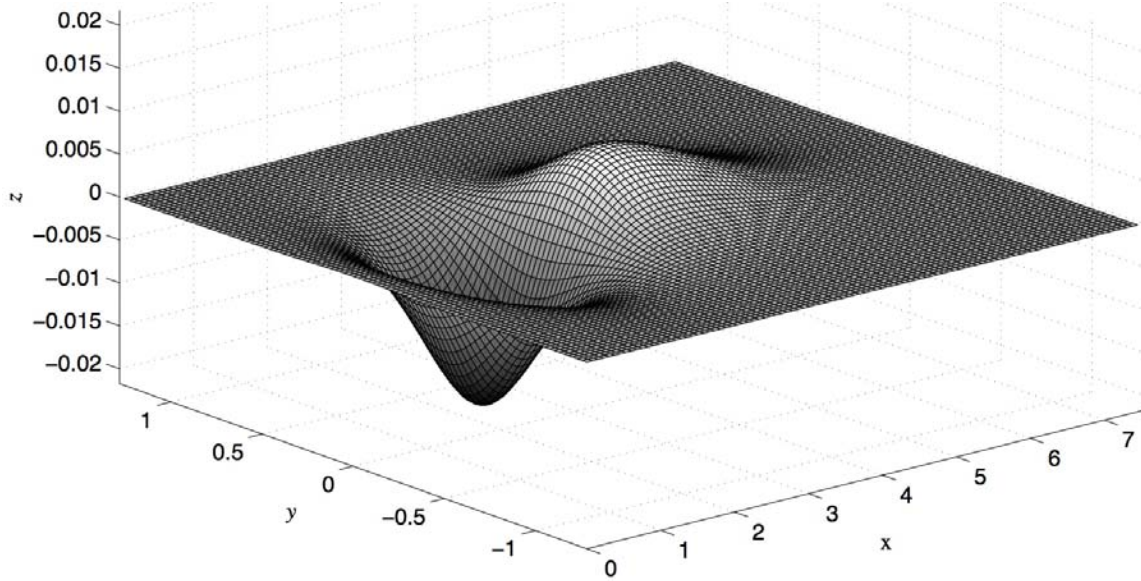

Fig. A12: Free surface elevation $\eta(x,y)$ at t_o, i.e., SMF tsunami source, from empirical tsunami source elevation Eq. A2.15, with parameterization of Eqs. A2.5 and A2.19-A2.23, for the case of Fig. A6, A11.
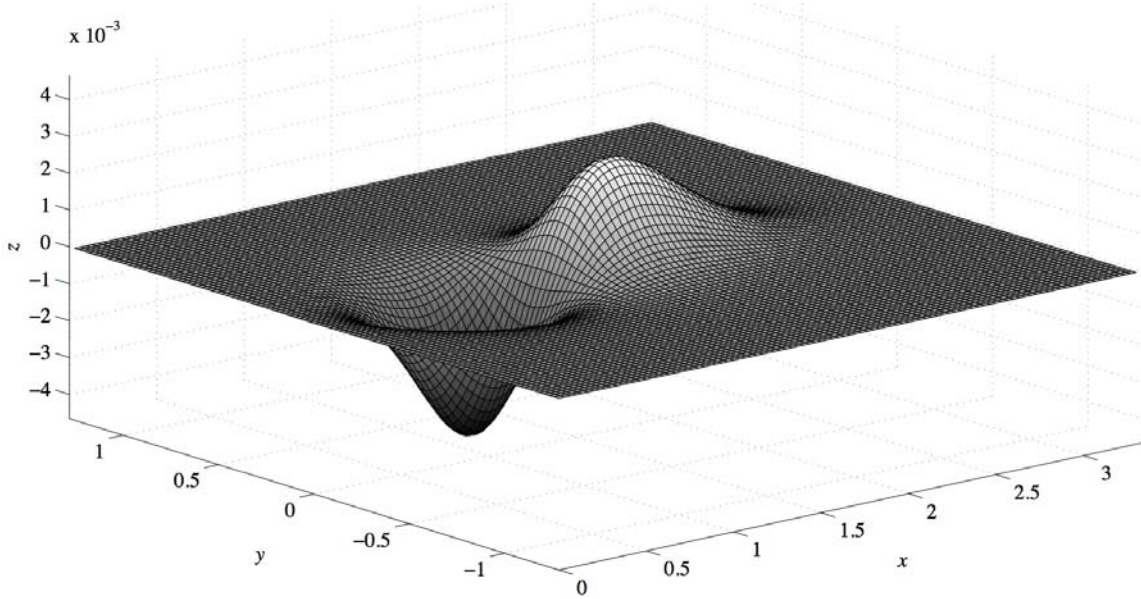
51

Since free surface elevations features at time t_o appear qualitatively similar in computations for slide or slumps (e.g., Grilli et al., 2002; Grilli and Watts, 2005), the same parameterization of the initial source elevation as for *slides* (described by Eq. A2.15, with η_o calculated by Eqs. A2.6-A2.8), is used for *slumps* as well. For the lateral spreading function *f(W)*, we use the new parameterization of Eq. A2.19. For the other parameters, we use the slump parameterization A2.18, which was more recently done in TOPICS and validated on a number of case studies (e.g., Tappin et al., 2008).

Fig. A.12, for instance shows the initial free surface calculated this way for a slump of geometry similar to the earlier slide, i.e., for the equivalent semi-ellipsoid: $B = 0.298$ m*, $T = 0.082$ m*, $W = 0.515$ m (Eqs. A2.10)*, density $\gamma = 2.435$ and an initial slide submergence $d = 0.120$ m on a 15 deg. slope (for which $x_o = 0.764$ m). Using $C_m = 0.685$, $\Delta\phi = 20$ deg. and a short slump displacement on the slope, $\Delta s = 2B = 0.496$ m, Eqs. A2.6-A2.8 yield, $R = 1.707$ m, $t_o = 615$ s, $s_o = 0.248$ m, $\eta_o = 0.0078$ m, $\eta_o^{3D} = 0.0032$ m, $f(W) = 0.407$, $\eta_{min} = -0.0039$ m ($f_1 = 1.22$), $\eta_{max} = 0.0024$ m ($f_2 = 0.76$), $x_{min} = 0.951$ m, $x_{max} = 11.551$ m, $\lambda_o = 0.667$ m.

3D Slide/slump tsunami source initial flow velocity

Initial velocity $\mathbf{u}(x,y)$ is specified for the semi-empirical 3D tsunami source elevations, on the basis of (depth-integrated) mass conservation for long waves. For linear long waves of celerity $c = (gh)^{1/2}$, one can show (e.g., Grilli, 1997), that in the direction of propagation, $|\mathbf{u}| \approx c\eta$, where $\eta(x,y)$ is the local free surface elevation. In the present case, one can estimate the local direction of propagation as the free surface steepest decent, $\mathbf{d} = \nabla\eta/|\nabla\eta|$.

6. REFERENCES

Abadie, S., C. Gandon, S.T. Grilli, R. Fabre, J. Riss, E. Tric, D. Morichon, and S. Glockner. 2009. 3D numerical simulations of waves generated by subaerial mass failures. Application to La Palma case. In *Proc. 31st Intl. Coastal Engng. Conf.* (J. McKee Smith, ed.) (ICCE08, Hamburg, Germany, Sept. 2008), pp. 1384—1395. World Scientific Publishing Co. Pte. Co.

Abadie, S., D. Morichon, S. Grilli, and S. Glockner. 2010. Numerical simulation of waves generated by landslides using a multiple-fluid Navier-Stokes model. *Coastal Engng.* 57: 779—794.

Abadie, S., J. Harris, and Grilli, S.T. 2011. Numerical simulation of tsunami generation by the potential flank collapse of the Cumbre Vieja Volcano. In *Proc. 21st Offshore and Polar Engng. Conf.* (ISOPE11, Maui, HI, June 19-25, 2011), Intl. Society of Offshore and Polar Engng.

Andrade, C., P. Borges, and M.C. Freitas. 2006. Historical tsunami in the Azores archipelago (Portugal). *Journal of Volcanology and Geothermal Research.* 156: 172–185.

Argus, D. F., R. G. Gordon, C. DeMets, and S. Stein. 1989. Closure of the Africa-Eurasia-North America plate motion circuit and tectonics of the Gloria fault. *J. Geophys. Res.* 94: 5585—5602.

Baptista, M. A., and C. Lemos. 2000. The source of the 1722 Algarve earthquake, inferred from hydrodynamic modeling of the associated tsunami. *European Geophysical Society, 25th general assembly.* Nice, France, April 25-29, 2000.

Barkan, R., U. S. ten Brink, and J. Lin. 2009. Far field tsunami simulations of the 1755 Lisbon earthquake: Implications for tsunami hazard to the U.S. East Coast and the Caribbean. *Marine Geology.* 264: 109-122.

Bent, A. L. 1994. *Seismograms for historic Canadian earthquakes: The 19 November 1929 Grand Banks earthquake.* Geological Survey of Canada, Open File Report 2563. 36 pp.

Bent, A. L. 1995. A complex double-couple source mechanism for the Ms 7.2 1929 Grand Banks earthquake. *Bulletin of the Seismological Society of America.* 85: 1003—1020.

Bryant, E. 2001. *Tsunami – the underrated hazard.* Cambridge: Cambridge University Press.

Buforn, E., A. Udias and M. A. Colombas. 1988. Seismicity, source mechanisms and tectonics of the Azores-Gibraltar plate boundary. *Tectonophysics.* 152: 89—118.

Caribbean Tsunami Hazard 2006. (Eds. A. Mercado-Irizarry and P.L.-F. Liu). World Sci. Pub., Singapore.

Chen, Q., J. T. Kirby, R. A. Dalrymple, A. B. Kennedy, and A. Chawla. 2000. Boussinesq modeling of wave transformation, breaking, and runup. II: 2-D. *J. Waterway, Port, Coastal and Ocean Engineering*. 126: 48—56.

U.S.G.S. 2001. *Earthquakes and Tsunamis in Puerto Rico and the U.S. Virgin Islands*. USGS Fact Sheet FS-141-00.

Day, S. J., P. Watts, S. T. Grilli, and J.T. Kirby. 2005. Mechanical Models of the 1975 Kalapana, Hawaii Earthquake and Tsunami. Marine Geology. 215(1-2): 59-92.

DeMets, C. 1993. Earthquake slip vectors and estimates of present-day plate motions. *J. Geophys. Res.* 98: 6703—6714.

Dolan, J. F., and Wald, D. J. 1998. The 1943-1953 north-central Caribbean earthquakes: Active tectonic setting, seismic hazards, and implications for Caribbean-North America plate motions. *Geological Society of America Special Publications*. 326: 143—170.

Driscoll, N. W., J. K.Weissel, and J. A. Goff. 2000. Potential for large-scale submarine slope failure and tsunami generation along the U.S. mid-Atlantic coast. *Geology*. 28(5): 407–410.

Dunbar, P. K. and C. S. Weaver. 2008. U.S. States and Territories National Tsunami Hazard Assessment: Historical Record and Sources for Waves. Prepared for the National Tsunami Hazard Mitigation Program by *NOAA* and *USGS*.

Enet, F, Grilli, S.T. and P. Watts, 2003. Laboratory Experiments for Tsunamis Generated by Underwater Landslides: Comparison with Numerical Modeling. In *Proc. 13th Offshore and Polar Engng. Conf.* (ISOPE03, Honolulu, USA, May 2003), 372-379.

Enet F. and S.T. Grilli 2005. Tsunami Landslide Generation: Modelling and Experiments. In *Proc. 5th Intl. on Ocean Wave Measurement and Analysis* (WAVES 2005, Madrid, Spain, July 2005), IAHR Publication, paper 88, 10 pps.

Enet, F. and S. T. Grilli. 2007. Experimental study of tsunami generation by three-dimensional rigid underwater landslides. *J. Waterway, Port, Coastal and Ocean Engineering..* 133: 442—454.

Fabre, R., E. Tric, J. Riss, T. Lebourg, and S. Abadie. New investigation of potential collapse of the Cumbre Vieja's volcanic ediface (La Palma Island; Spain); numerical evaluation of failure and estimated volume. In revision.

Fine, I.V., A.B. Rabinovich, B.D. Bornhold, R. E. Thomson, and E.A. Kulikov. 2005. The Grand Banks landslide-generated tsunami of November 18, 1929: Prelaminary analysis and numerical modeling. *Marine Geology*. 215: 45-57.

Fryer, G. L., P. Watts, and L. F. Pratson. 2004. Source of the great tsunami of 1 April 1946: A landslide in the upper Aleutian forearc. *Marine Geology*. 203: 201-218.

Gica, E., M. C. Spillane, V. V. Titov, C. D. Chamberlin, and J. C. Newman. 2008. Development of the forecast propagation database for NOAA's Short-Term Inundation Forecast for Tsunamis (SIFT). NOAA Tech. Memo. OAR PMEL-139.

Geist, E. L., P. J. Lynett and J. D. Chaytor. 2009. Hydrodynamic Modeling of Tsunamis from the Currituck Landslide. *Marine Geology*. 264: 41-52.

Gisler G., Weaver R., Gittings M.L., 2006. Sage calculations of the tsunami threat from La Palma. Science *of Tsunami Hazard*, 24(4): 288-301.

Gracia, E., J. Dañobeitia, J. Vergés, and PARSIFAL Team. 2003. Mapping active faults offshore Portugal (36 degrees N – 38 degrees N); implications for seismic hazard assessment along the Southwest Iberian margin. *Geology*. 32: 83—86.

Grandin, R., J. F. Borges, M. Bezzeghoud, B. Caldeira, and F. Carrilho. 2007. Simulations of strong ground motion in SW Iberia for the 1969 February 28 (Ms=8.0) and the 1755 November 1 (M~ 8.5) earthquakes – I. Velocity model. II. Strong ground motion simulations. *Geophysical Journal International*. 171(2): 807—822.

Greene, H. G., Murai, L. Y., Watts, P., Maher, N. A., Fisher, M. A., Paull, C. E., and Eichhubl, P. 2006. Submarine landslides in the Santa Barbara Channel as potential tsunami sources. *Nat. Hazards and Earth Sci. Systems*. EGU. 6: 63-88.

Grilli, S.T. 1997. Fully Nonlinear Potential Flow Models used for Long Wave Runup Prediction. Chapter in *Long-Wave Runup Models,* (eds. H. Yeh, P. Liu, and C. Synolakis), pps. 116-180. World Scientific Publishing, Singapore.

Grilli, S. T. and P. Watts. 1999. Modeling of waves generated by a moving submerged body. Applications to underwater landslides. *Engng. Anal. Bonud. Elem.* 23: 645—656.

Grilli, S.T., S. Vogelmann, and P. Watts. 2002. Development of a 3D numerical wave tank for modeling tsunami generation by underwater landslides. *Engng. Anal. Bound. Elem.* 26: 301—313.

Grilli, S.T. and P. Watts 2001 Modeling of tsunami generation by an underwater landslide in a 3D-NWT. In *Proc. 11th Offshore and Polar Engng. Conf.* (ISOPE01, Stavanger, Norway, June 2001), Vol III, 132-139.

Grilli, S. T., and P. Watts. 2005. Tsunami generation by submarine mass failure. Part I: Modeling, experimental validation, and sensitivity analysis. *J. Waterway, Port, Coastal and Ocean Engineering.* 131: 283—297.

Grilli, S. T., C. D. P. Baxter, S. Maretzki, Y. Perignon, and D. Gemme. 2006. Numerical simulation of tsunami hazard maps for the US East Coast. Tech. rep., FM Global Project.

Grilli, S. T., M. Ioualalen, J.Asavanant, F. Shi, J. Kirby, and P. Watts. 2007. Source Constraints and Model Simulation of the December 26, 2004 Indian Ocean Tsunami. *J. Wtrwy, Port, Coast, and Oc. Engrg.* ASCE. 133(6): 414-428.

Grilli, S. T., S. Dubosq, N. Pophet, C. D. P. Baxter, and O.-D. S. Taylor. 2008. Numerical simulation of tsunami runup and flooding on the North Shore of Puerto Rico. Tech. Rep., FMGlobal Project.

Grilli. S.T., O.-D. S. Taylor, D.P. Baxter, and S. Maretzki. 2009. Probabilistic approach for determining submarine landslide tsunami hazard along the upper East Coast of the United States.Marine Geology. 264(1-2): 74-97.

Grilli, S. T., S. Dubosq, N. Pophet, Y. Pérignon, J. T. Kirby, and F. Shi. 2010a. Numerical simulation and first-order hazard analysis of large co-seismic tsunamis generated in the Puerto Rico trench: near-field impact on the North shore of Puerto Rico and far-field impact on the US East Coast, *Nat. Hazards Earth Syst. Sci.*, 10: 2109–2125.

Grilli, S.T., Dias, F., Guyenne, P., Fochesato, C. and F. Enet 2010b. Progress In Fully Nonlinear Potential Flow Modeling Of 3D Extreme Ocean Waves. Chapter 3 in *Advances in Numerical Simulation of Nonlinear Water Waves* (ISBN: 978-981-283-649-6, edited by Q.W. Ma) (Vol. 11 in Series in Advances in Coastal and Ocean Engineering). World Scientific Publishing Co. Pte. Ltd., pps. 75- 128.

Grimison, N. L., and W. Chen. 1986. The Azores-Gibraltar plate boundary: Focal mechanisms, depth of earthquakes and their tectonical implications. *J. Geophys. Res.* 91: 2029—2047.

Gutscher M. A., M.A. Baptista, J.M. Miranda. 2006.The Gibraltar Arc seismogenic zone (part 2): Constraints on a shallow east dipping fault plane source for the 1755 Lisbon earthquake provided by tsunami modeling and seismic intensity. *Tectonophysics*. 426: 153–166.

Hanks, T. C. and H. Kanamori. 1979. A moment magnitude scale. *J. Geophys. Res.* 84: 2348-2350.

Hayward, N., A. B. Watts, G. K. Westbrook, and J. S. Collier. 1999. A seismic reflection and GLORIA study of compressional deformation in the Gorringe Bank region, eastern North Atlantic. *Geophys. J. Intl.* 138: 831-850.

Ioualalen, M., B. Pelletier, P. Watts, and M. Regnier. 2006. Numerical modeling of the 26th November 1999 Vanuatu tsunami.*J. Geophys. Res*. 111(C6): 2005JC003249.

Ioualalen, M., J. Asavanant, N. Kaewbanjak, S. T. Grilli, J. T. Kirby, and P.Watts, 2007. Modeling the 26 December 2004 Indian Ocean tsunami: Case study of impact in Thailand. *J. Geophys. Res*. 112: 2006JC003850.

Ioualalen, M., S. Migeon, and O. Sardoux. 2010. Landslide tsunami vulnerability in the Ligurian Sea: case study of the 1979 October 16 Nice international airport submarine landslide and of identified geological mass failures, *Geophys. J. Intl.* 181:724–740, doi:10.1111/j.1365-246X.2010.04572.

Johnston, A. 1996. Seismic moment assessment of earthquakes in stable continental regions–III. New Madrid 1811-1812, Charleston 1886 and Lisbon 1755. *Geophysical Journal International*. 126: 314—344.

Kennedy, A. B., Q. Chen, J. T. Kirby, and R. A. Dalrymple. 2000. Boussinesq modeling of wave transformation, breaking and runup: I. One dimension. *Journal of Waterway, Port, Coastal, and Ocean Engineering*. 126: 39—47.

Kirby, J. T. 2003. Boussinesq models and applications to nearshore wave propagation, surf zone processes and wave-induced currents. In *Advances in Coastal Modeling, and Oceanography.* V. C. Lakhan (Editor). Elsevier, New York. 67: 1—41.

Kirby, J. T., N. Pophet, F. Shi, and S. T. Grilli. 2009. Basin scale tsunami propagation modeling using Boussinesq models: Parallel implementation in spherical coordinates. In *Proc. WCCE-ECCE-TCCE Joint Conf. on Earthquake and Tsunami.* Istanbul, Turkey, June 22-24, 2009.

Knight, B. 2006. Model predictions of Gulf and southern Atlantic coast tsunami impacts from a distribution of sources. *Science of Tsunami Hazards.* 24(5): 304—312.

Lander, J. F., L. S. Whiteside, and P. A. Lockridge, 2002. A Brief History of Tsunamis in the Caribbean Sea. *Science of Tsunami Hazards.* 20 (1) 57-94.

Lee, H.J. 2009. Timing occurrence of Large Submarine Landslides on the Atlantic Ocean Margin. Marine Geology. 264: 53-64.

Locat J., H. Lee, U. S. ten Brink, D Twichell, E. Geist, and M. Sansoucy. 2009. Geomorphology, stability and mobility of the Currituck slide. *Marine Geology.* 264: 28—40.

Lockridge, P. A., L. S. Whiteside, and J. F. Lander. 2002. Tsunamis and tsunami-like waves of the Eastern United States. *Science of Tsunami Hazards.* 20(3): 120—157.

Løvholt, F., G. Pedersen, and G. Gisler. 2008. Oceanic propagation of a potential tsunami from the La Palma Island. *J. Geophys. Res.* 113: C09026, doi:10.1029/2007JC004603.

Mader, C. L., 2001 Modeling the La Palma landslide tsunami. *Science of Tsunami Hazards.* 19: 150-170.

Masson, D. G., A. B. Watts, M. J. R. Gee, R. Urgeles, N. C. Mitchell, T. P. Le Bas, and M. Canals. 2002 Slope failures on the flanks of the western Canary Islands. *Earth-Science Reviews.* 57: 1—35.

Masson, D. G., C. B. Harbitz, R. B. Wynn, G. Pedersen, and F. Lovholt. 2006. Submarine landslides: Processes, triggers, and hazard prediction. *Philosophical Transactions of the Royal Society A.* 264: 2009—2039.

McMurtry, G. M., D. R. Tappin, P. N. Sedwic, I Wilkinson, J. Fietzke, and B. Sellwoo. 2007. Elevated marine deposits in Bermuda record a late Quaternary megatsunami. *Sedimentary Geology.* 200: 155—165.

Mercado, A. and W. McCann. 1998. Numerical Simulation of the 1918 Puerto Rico Tsunami. *Natural Hazards.* 18: 57–76.

Moss, J.L., W.J. McGuire, and D. Page. 1999. Ground deformation monitoring of a potential landslide at La Palma, Canary Islands, *J. Volcanology and Geothermal Research.* 94: 251-265.

Nikolkina I., N. Zahibo and E. Pelinovsky. 2010. Tsunami in Guadeloupe (Caribbean Sea). *The Open Oceanography Journal.* 4: 44-49.

Okada, Y. 1985. Surface deformation due to shear and tensile faults in a half-space. *B. Seismol. Soc. Am.* 75(4): 1135—1154.

O'Loughlin, K.F. and Lander, J.F. *Caribbean Tsunamis: A 500-Year History from 1498–1998.* Advances in Natural and Technological Hazards Research, V. 20, Klüwer, 2003.

Pararas-Carayannis, G. 2002. Evaluation of the threat of mega tsunami generation from postulated massive slope failures of island stratovolcanoes on La Palma, Canary Islands, and on the island of Hawaii. *Science of Tsunami Hazards.* 20(5): 251—277.

Perignon, Y. 2006. Tsunami hazard modeling. Tech. rep., Department of Ocean Engineering, University of Rhode Island and Ecole Centrale de Nantes.

Pophet, N., 2008. *Parallel computation for tsunami.* M.S. Thesis, Chulalongkorn University.

Pophet, N., Ioualalen, M., Asavanant, J., 2010. Parallelization of fully nonlinear Boussinesq equations for tsunami simulations: new approach on higher grid resolution for tsunami simulation using parallelized fully nonlinear Boussinesq Equations. *Computers and Fluids…*

Prior, D. B., E. H. Doyle, and T. Neurauter. 1986. The Currituck Slide, Mid-Atlantic continental slope; revisited. *Marine Geology.* 73: 25—45.

Rahiman, T. I. H., J. R. Pettinga, and P. Watts. 2007. The source mechanism and numerical modelling of the 1953 Suva tsunami, Fiji. *Marine Geology.* 237(2): 55-70.

Ruffman, A. 2005. Comment on: Tsunamis and Tsunami-like of the Eastern United States by Patricia A. Lockridge, Lowell S. Whiteside and James Lander with Respect to The November 18, 1929 Earthquake and Its Tsunami. *Science of Tsunami Hazards.* 23(3): 52-59.

Sykes, L. R., W. McCann, and A. Kafka. 1982. Motion of Caribbean plate during the last 7 million years and implications for earlier cenozonic movements. *J. Geophys. Res.* 70: 5065—5074.

Tappin, D. R., P. Watts and S. T. Grilli. 2008. The Papua New Guinea tsunami of July 17, 1998: Anatomy of a catastrophic event. *Nat. Haz. and Earth Sys. Sci.,* 8: 243-266.

ten Brink, U. S. and J. Lin. 2004. Stress interaction between subduction earthquakes and forensic strike-slip faults: Modeling and application to the northern Caribbean plate boundary. *J. Geophys. Res.* 109, B12310.

ten Brink, U. S. 2005. Vertical motions in the Puerto Rico trench and Puerto Rico and their cause. *J. Geophys. Res.* 100: B06404.

ten Brink, U. S., D. Twichell, E. Geist, J. Chaytor, J. Locat, H. Lee, B. Buczkowski, and M. Sansoucy 2007. The Current State of Knowledge Regarding Potential Tsunami Sources Affecting U.S. Atlantic and Gulf Coasts. Report to the Nuclear Regulatory Commission. *USGS*. 166 pages.

ten Brink, U. S., D. Twichell, E. Geist, J. Chaytor, J. Locat, H. Lee, B. Buczkowski, R. Barkan, A. Solow, B. Andrews, T. Parsons, P. Lynett, J. Lin, and M. Sansoucy. 2008. Evaluation of Tsunami Sources with the Potential to Impact the U.S. Atlantic and Gulf Coasts. Report to the Nuclear Regulatory Commission. *USGS*. 322 pages.

ten Brink, U. S., H. J. Lee , E. L. Geist, and D. Twichell. 2009a. Assessment of tsunami hazard to the U.S. East Coast using relationships between submarine landslides and earthquakes. *Marine Geology*. 264: 65–73.

ten Brink, U.S., R. Barkan, B.D. Andrews, and J.D. Chaytor. 2009b. Size distributions and failure initiation of submarine and subaerial landslides. *Earth and Planetary Science Letters*. 287: 31–42.

Twichell, D. C., J. D. Chaytor, U.S. ten Brink, and B. Buczkowski. 2009, Morphology of Late Quaternary Submarine Landslides along the U.S. Atlantic Continental Margin. *Marine Geology*. 264: 4-15.

U.S.G.S. April 2001. Earthquakes and Tsunamis in Puerto Rico and the U.S. Virgin Islands. USGS Fact Sheet FS–141–00

Walder, J.S., P. Watts, and C.F. Waythomas. 2006. Mapping tsunami hazards associated with debris flow into a reservoir. *J. Hyd. Eng.* ASCE. 132(1): 1-11.

Ward S. N. 2001.Tsunamis. *Encyclopedia of Physical Science and Technology* .175-191,

Ward, S. N. and S. Day. 2001. Cumbre Vieja Volcano – potential collapse and tsunami at La Palma, Canary Islands. *Geophys. Res. Lett.* 21: 397—400.

Watts, P. and Grilli, S.T., 2003. Tsunami Generation by Deformable Underwater Landslides. In *Proc. 13th Offshore and Polar Engng. Conf.* (ISOPE03, Honolulu, USA, May 2003), 364-371.

Watts, P., S. T. Grilli, J. T. Kirby, G. J. Fryer, and D. R. Tappin. 2003. Landslide tsunami case studies using a Boussinesq model and a fully nonlinear tsunami generation model. *Nat. Hazards Earth Syst. Sci.* 3: 391—402.

Watts, P., S. T. Grilli, D. Tappin, and G. J. Fryer. 2005. Tsunami generation by submarine mass failure. Part II: predictive equations and case studies. *J. Waterw. Port, Coast. Ocean Engng.* 131: 298—310.

Watts, P. 2006. Case study of the 1755 Portugal tsunami. Final report for Risk Management Solutions, Inc.

Waythomas, C. F., P. Watts, and , J. S. Walder. 2006. Numerical simulation of tsunami generation by cold volcanic mass flows at Augustine volcano, Alaska. *Nat. Haz. And Earth Sys. Sci.* NHESS. 6: 671-685.

Wei, G., and J. T. Kirby. 1995. Time-dependent numerical code for extended Boussinesq equations. *J. Wtrwy, Port, Coast, and Oc. Engrg.* ASCE. 121(5): 251-261.

Wei, G., J. T. Kirby, S. T. Grilli, and R. Subramanya. 1995. A fully nonlinear Boussinesq model for free surface waves. Part 1: Highly nonlinear unsteady waves. *J. Fluid Mech.* 294: 71-92.

Wynn, R. B. and D. G. Masson. 2003. Canary Island landslides and tsunami generation: can we use turbidite deposits to interpret landslide processes? *In* Locat, J., and J. Meinert (Editors), Submarine mass movements and Their Consequences, Kluwer, Dordrecht. 325—332.

Zahibo, N. and E. N. Pelinovsky. 2001. Evaluation of tsunami risk in the Lesser Antilles. *Natural Hazards and Earth System Sciences.* 1: 221–231.

Zahibo, N., E. Pelinovsky, A. Yalciner, A. Kurkin, A. Koselkov, and A. Zaitsev, 2003a. The 1867 Virgin Island Tsunami: observations and modeling. *Oceanologica Acta.* 26: 609—621.

Zahibo N., E. Pelinovsky, A. Kurkin, and A. Kozelkov. 2003b. Estimation of far-field tsunami potential for the Caribbean coast based on numerical simulation. *Science of Tsunami Hazards.* 21 (4): 202-222.